

**Evaluating different deep learning models for efficient extraction of Raman signals from CARS spectra**

Journal:	<i>Physical Chemistry Chemical Physics</i>
Manuscript ID	CP-ART-04-2023-001618.R1
Article Type:	Paper
Date Submitted by the Author:	n/a
Complete List of Authors:	Junjuri, Rajendhar; Lappeenranta University of Technology, School of Engineering Science; Leibniz Institute of Photonic Technology, Photonic data science Saghi, Ali; Lappeenranta University of Technology, LUT School of Engineering Science Lensu, Lasse; Lappeenranta University of Technology, LUT School of Engineering Science Vartiainen, Erik; Lappeenranta University of Technology, Engineering Science

SCHOLARONE™  
Manuscripts



Physical Chemistry Chemical Physics



## Guidelines for Reviewers



Thank you very much for your agreeing to review this manuscript for [Physical Chemistry Chemical Physics \(PCCP\)](#).

PCCP is an international journal for the publication of cutting-edge original work in physical chemistry, chemical physics and biophysical chemistry, spanning experiment, theory, computation and data science. To be suitable for publication in PCCP, articles must include significant innovation and/or insight into physical chemistry; this is the most important criterion that reviewers and the Editors will judge against when evaluating submissions. Further information on our scope can be found at [rsc.li/pccp](https://rsc.li/pccp).

PCCP's Impact Factor is **3.945** (2021 Journal Citation Reports®)

*The following manuscript has been submitted for consideration as a*

## PAPER

Full papers should contain original scientific work that has not been published previously. Full papers based on Communications are encouraged provided that they represent a substantial extension of the original material. There are no restrictions on the length of a paper. Authors should include a brief discussion in the Introduction that sets the context for the new work and gives their motivation for carrying out the study.

When preparing your report, please:

- Focus on the originality, importance, impact and reliability of the science. English language and grammatical errors do not need to be discussed in detail, except where it impedes scientific understanding.
- Use the [journal scope and expectations](#) to assess the manuscript's suitability for publication in PCCP.
- State clearly whether you think the article should be accepted or rejected and include details of how the science presented in the article corresponds to publication criteria.
- Inform the Editor if there is a conflict of interest, a significant part of the work you cannot review with confidence or if parts of the work have previously been published.

Best regards,

**Professor Anouk Rijs**  
Editorial Board Chair  
Vrije Universiteit Amsterdam, The Netherlands

**Dr Michael A. Rowan**  
Executive Editor  
Royal Society of Chemistry

Contact us

Please visit our [reviewer hub](#) for further details of our processes, policies and reviewer responsibilities as well as guidance on how to review, or click the links below.



### **Detailed Response to Reviewers**

We thank the reviewers for their detailed reading and for suggesting improvements to the manuscript. We have addressed all the suggestions and queries presented by the reviewers as given in the following sections.

#### **Reviewer 1**

**The study evaluated four deep learning models (CNN, LSTM, VECTOR, and Bi-LSTM) to retrieve the Raman signals from the CARS spectra. All models were trained with CARS data generated by simulations and tested on three non-resonant background signals. Results showed that Bi-LSTM outperformed the other three models regarding mean square error, ability to extract spectral lines, and correlation analysis. The study also confirmed the Bi-LSTM model's superior predictive capability on experimental samples. The work done is novel and extremely useful. The authors are requested to revisit their work and work on the questions below to improve the manuscript's quality.**

We thank the reviewer for the careful evaluation of the manuscript.

- 1. The authors should cite some of the earlier works and provide a perspective for the present work. For example, see,**

- 1. Optics Express, Vol. 30, Iss. 15, p.26057-26071 (2022).**
- 2. Optics Continuum, Vol. 1, Iss. 6, p.1324-1339 (2022).**
- 3. <https://doi.org/10.1063/5.0007821>**

We have added the first reference as per the reviewer's suggestion which was missed in the first submission. However, the second and third references were already cited in the original manuscript. The reference numbers are 31 and 33, respectively, in the revised manuscript.

- 4. The work done using the VECTOR model earlier by Wang et al. (<https://doi.org/10.1002/jrs.6335>) reported mean absolute error (MAE) as an accuracy measure and reported an MAE of ~0.005 as a function of the number of vectors. The current work has used mean square error as a loss function and a measure hence absolute comparison is difficult. However, the VECTOR model reported earlier is equally good, and the authors must emphasize the merits of the Bi-LSTM.**

We have compared results obtained from different DL models (without modifying their original architectures) where their hyperparameters were already optimized by various research groups. Also, in all our previous works, we have used mean square error (MSE) as a metric to compare the results. Hence, we have followed the same here to properly visualize the results and demonstrated superior performance compared to previous studies. It is also worth considering that the training and testing data are different for the original VECTOR and the newly proposed Bi-LSTM. Hence, direct head-to-head comparison of the metric (MAE) is not feasible. The same is already mentioned by the reviewer.

However, as suggested by the reviewer, we have estimated the MAE obtained from 300 test spectra for all four models, as shown in below Figure 1. It is evident from the figure the Bi-LSTM model still has the edge over all the other models, where it has shown 6 times less MAE. It has also demonstrated superior performance for the experimental data, where it could retrieve the Raman signal on edges contrary to the other models.

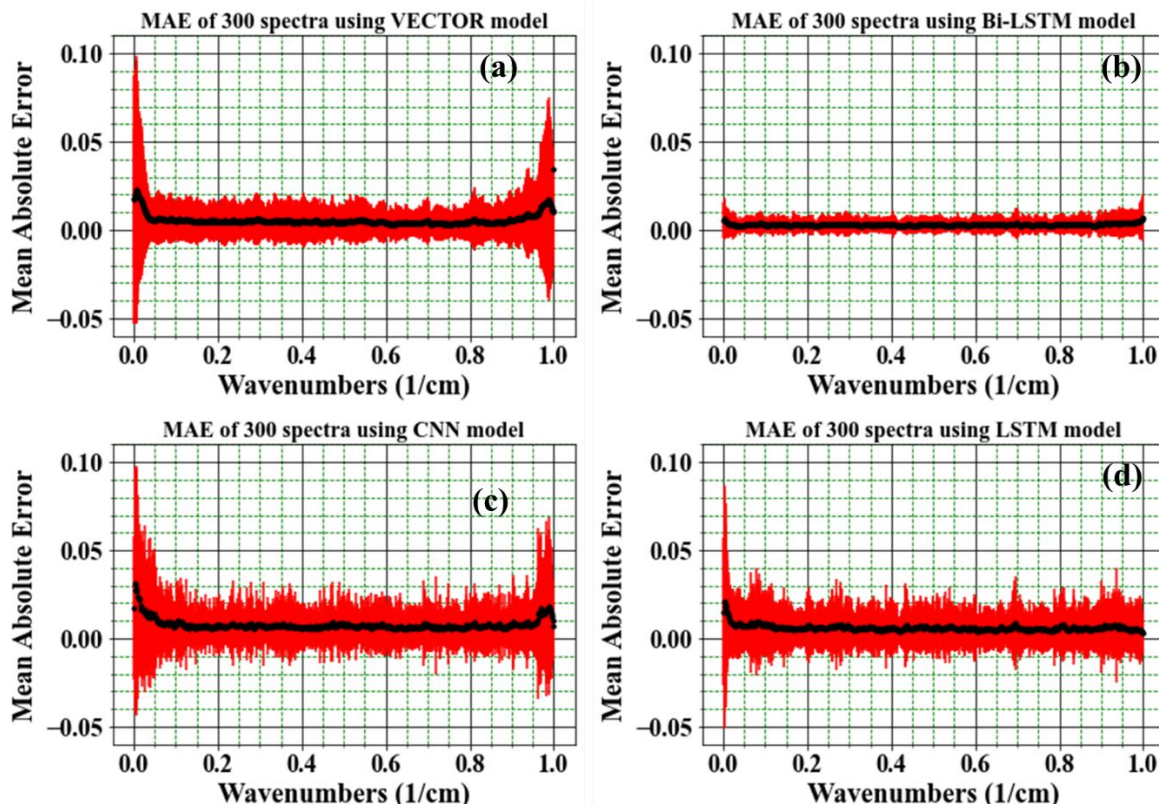


**Figure 1.** Mean absolute error (MAE) obtained from 300 test spectra for all the four models. (The same figure is included in supplementary data as figure 5 and it also mentioned in the revised manuscript).

5. **Using the same optimizer function while comparing different DNN architectures to rule out the benefit originating purely from the optimizer function rather than the architecture is good. For example, in the CNN and LSTM architectures, Adam was used as an optimizer while in Bi-LSTM, Nadem was used, making the comparison inadequate. The optimizer for the VECTOR architecture should be mentioned.**

We used the original optimizer proposed for each model. For example, stochastic gradient descent (SGD) was applied for the VECTOR model. Relevant details of all the models are now presented in the supplementary document in Table 1. The reason for using the originally proposed optimizer is that using another one would have caused the need to tune the training process, and likely, a hyperparameter optimization procedure would have been necessary. However, we will consider the reviewer's suggestion to compare the results purely based on the optimizer in future studies.

6. **The input data was said to be 640 data points (wavenumbers) from the simulated data. However, in the case of experimental data, it is difficult to get the same number of data points for the samples studied in this work. Figure 7 also indicates that the data collected for each sample is in different ranges. Hence, discussing how this has been taken care of while testing the model is helpful.**

Yes, this is true that the need to use only 640 wavenumber data points is a limitation. However, for Raman data, this is enough to provide a good spectral resolution and a wide enough range. For instance, the protein samples' spectra were evaluated in two separate regions,  $700 - 1900 \text{ cm}^{-1}$  and  $1900 - 3100 \text{ cm}^{-1}$ . So, in both cases, the width of the spectral range was the same ( $1200 \text{ cm}^{-1}$ ), as also the spectral resolution ( $< 2 \text{ cm}^{-1}$ ).

7. **In figure 8 a1, a2, please plot the squared error on a smaller scale to see the variation to be easy to quantify (as done for b1 and b2).**

We have modified the y-axis scale in the squared error plot, and the error is visualized correctly now.

**8. In some instances, Bi-LSTM has been referred to as BI-LSTM. Please check and correct.**

We have now replaced the acronym in the revised manuscript.

**9. It is discussed that the LSTM model for the simulated data has shown a lower standard deviation relative to the VECTOR model, as communicated in Fig 3. However, for the case of experimental samples and especially yeast, the deviation of LSTM is significantly higher than the VECTOR model. Please explain.**

The LSTM model has shown a lower standard deviation of 0.01 compared to the VECTOR only for a few points on the left side of the spectra, corresponding to less than 5 % of the total data. Further, it is also worth considering that the LSTM has given an error of more than 0.01 for 90 % of the spectral region. In contrast, it is close to zero for the VECTOR model, as shown in Figure 3 in the revised manuscript. These observations are reflected in correlation measurements of the simulated data, where 172 spectra have a correlation of more than 0.98 compared to 131 spectra for LSTM, as shown in Figure 5 in the revised manuscript. These observations indicate that the VECTOR has superior performance compared to LSTM.

**10. Though the Pearson Correlation Coefficient for models other than Bi-LSTM is much lower than the ideal number of 1 for the simulated data (Fig 5), for the experimental data, the performance of VECTOR, Bi-LSTM and CNN are almost comparable (Fig 9). Explain this drastic positive difference in the performance of the experimental data.**

The Bi-LSTM model has very well predicted the minimum intensity lines in the simulated data. It also correctly retrieved the data at both ends of the spectral range. These are the likely grounds for achieving very high correlation coefficients for the simulated data. Similar observations are also noticed in the experimental data. A closer view of the figure shows that a higher correlation with lower error is obtained for the Bi-LSTM compared to the others, as shown in below Figure 2. However, more experimental spectra are required for robust statistics like simulated data.

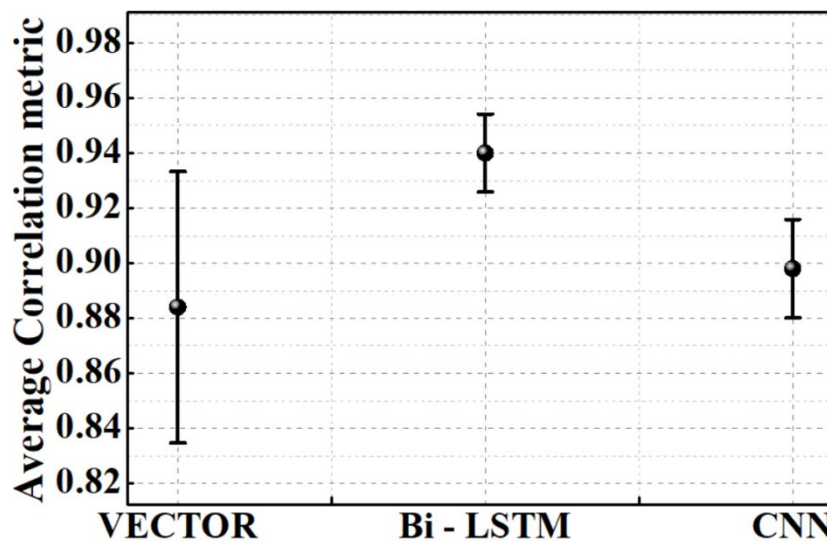


**Figure 2.** Closer view of the average value of the PCCs estimated from the five experimental CARS data.

**11. Sub-figures in Figure 1 are labelled as capital letters but referred to as small in the description. Please correct.**

We have edited the figure in the revised manuscript, and the labels have been changed to lowercase.

## 12. What is the time taken to run each of the models?

We have now measured the computational time for all four models. Also, the text presented below is included in supplementary data. (*This information also briefly mentioned in the revised manuscript in relevant sections to help readers*)

"The key characteristics of the models were kept the same as in the original articles, and they are shown in Figure 1 in the manuscript. The models were trained and tested on a computer with an i5-11320H @ 3.20GHz, 12.0 GB RAM. The training times of the models differ significantly, as shown in below Table 1. Bi-LSTM and LSTM have long training times, although they contain much less parameters than the CNN and VECTOR models. In an LSTM architecture, each node is composed of 4 gates, including forget gate, input gate, output gate, and cell state, which all have their computation processes. Therefore, more calculations are needed in each node when compared with the regular ANN nodes. In a Bi-LSTM model, input data flows in both directions through a bidirectional LSTM layer, so the computing time is increased. Also, the architecture contains an order of magnitude more parameters than the standard LSTM. In the case of VECTOR architecture, the large number of parameters in the encoders and decoders affect the training time. The inference times per sample are short, and the differences may be relevant in selected applications."

Table 1. Details of the computational parameters and times. Means square error (MSE) and mean absolute error (MAE) are loss functions. Stochastic gradient descent (SGD) is an optimizer for the VECTOR model.

S. No	Model	Loss Function	Optimizer	Parameters	Training time [h]	Testing time [ms]
1	CNN	MSE	Adam	6,016,932	0.8	$77.1 \pm 14.4$
2	LSTM	MAE	Adam	3,871	5.6	$83.7 \pm 18.2$
3	Bi-LSTM	MSE	Nadam	51,421	29.8	$238.7 \pm 22.5$
4	VECTOR	MAE	SGD	178,942,720	12.6	$51.6 \pm 12.3$

## 13. Neural networks tend to overfit the data. In this regard, looking at the learning curves of test/validation data sets and the training data sets is helpful. These learning curves are useful in diagnosing the models and analyzing their convergence. The authors can try plotting them and include them in the SI file.

The learning curves of the four deep learning models are shown in Figure 4 in the supplementary data. Also, the following text is presented in the supplementary document.

"The learning curves of the four deep learning models are shown in Figure 4. It should be noted that the magnitudes of the loss value in the plots are different. The training loss values are the batch loss averages within each epoch. In contrast, the validation loss values are the loss averages of the validation set using the current model. Therefore, in most cases, the validation loss is smaller than the training loss. To complement, dropout is used with the CNN and Bi-LSTM models affecting the training but not inference. The models' training processes converge differently. It is evident that with an appropriate criterion, early stopping of the training process could be adopted without affecting the model performance. This would also affect the training time, especially in the case of VECTOR, but also with the CNN and Bi-LSTM models. (*This information also briefly mentioned in the revised manuscript in relevant section to guide readers*)

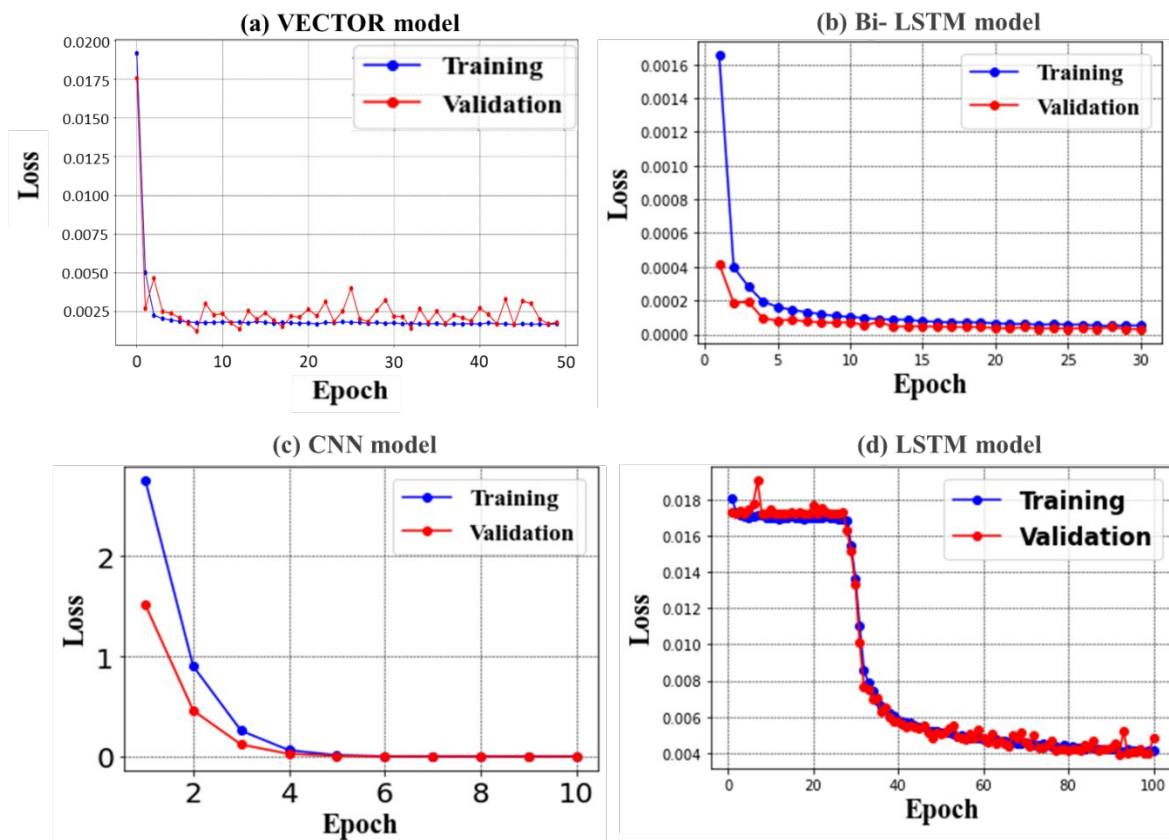


**Figure 4.** (a-d) Represent the learning curves of LSTM, Bi-LSTM, CNN, and VECTOR models respectively.

## Reviewer 2

The article gives a very thorough comparison of various deep learning algorithm applied to removal of the non-resonant background in CARS microscopy. Also a new variant is introduced Bi-LSTM that outperforms 4 others. The analysis is careful and complete. The article could use a little editing of the English and is maybe a bit long but this has the advantage that all the details can be seen.

We thank the reviewer for evaluating the manuscript. We have corrected the typos and checked the grammar.

## REFERENCES:

- C. H. Camp, Raman signal extraction from CARS spectra using a learned-matrix representation of the discrete Hilbert transform, *Opt. Express*, 2022, **30**, 26057–26071.

## ARTICLE

## Evaluating different deep learning models for efficient extraction of Raman signals from CARS spectra

Received 00th January 20xx,  
Accepted 00th January 20xx

DOI: 10.1039/x0xx00000x

Rajendhar Junjuri,<sup>a,b, #\*</sup> Ali Saghi <sup>#a</sup>, Lasse Lensu <sup>a</sup> and Erik M. Vartiainen <sup>a</sup>

The non-resonant background (NRB) contribution to the Coherent anti-Stokes Raman scattering (CARS) signal distorts the spectral line shapes and thus degrades the chemical information. Hence, finding an effective approach for removing NRB and extracting resonant vibrational signals is a challenging task. In this work, Bi-directional LSTM (Bi - LSTM) neural network is explored for the first time to remove NRB in CARS spectra automatically and, the results are compared with the three DL models reported in the literature viz, convolutional neural network (CNN), Long short-term memory (LSTM) neural network, very deep convolutional autoencoders (VECTOR). The results of the synthetic test data have shown that the Bi - LSTM model accurately extracts the spectral lines throughout the range. In contrast, the other three models' efficiency deteriorated while predicting the peaks on either end of the spectra, which resulted in a 60 times higher mean square error than the Bi - LSTM model. The Pearson correlation analysis demonstrated that Bi-LSTM model performance stands out from the rest, where 94 % of the test spectra have correlation coefficients of more than 0.99. Finally, these four models were evaluated on the four complex experimental CARS spectra viz, Protein, Yeast, DMPC, and ADP, where the Bi - LSTM model has shown superior performance, followed by CNN, VECTOR, and LSTM. This comprehensive study provides a giant leap toward simplifying the analysis of complex CARS spectroscopy and microscopy.

### 1. Introduction

The spontaneous Raman spectroscopic technique measures the vibrational response of molecules and provides functional and compositional information on the major chemical constituents. However, the acquired Raman signal strength is weak and, combined with the fluorescence contributions, results in longer acquisition times, limiting its applications. In contrast, Coherent anti-Stokes Raman scattering (CARS) is a nonlinear analytical method that offers similar fingerprint information to the spontaneous Raman technique, albeit orders of magnitude faster<sup>1,2</sup>. This characteristic property enabled it as a prominent spectroscopic tool for the label-free imaging of cells<sup>3</sup> and tissues<sup>4</sup> in biomedical applications<sup>5</sup>. Also, it has been significantly explored in other applications, such as materials science and nanotechnology. The intensity of the CARS signal is proportional to the susceptibility term and can be expressed as

$$I_{\text{CARS}} \propto |\chi_{\text{NR}}^{(3)} + \chi_R^{(3)}(\omega)|^2 \quad (1)$$

Here,  $\chi_{\text{NR}}^{(3)}$ ,  $\chi_R^{(3)}$  corresponds to the non-resonant and resonant third-order susceptibilities, respectively. As CARS being a coherent phenomenon the  $\chi_{\text{NR}}^{(3)}$ ,  $\chi_R^{(3)}$  responses of the sample

interfere via eq 1, and thus, the non-resonant background (NRB) contribution cannot be removed by simple subtraction. The NRB serves as a stable homodyne amplifier which is responsible for the signal strength of CARS. Nevertheless, this coherent contribution simultaneously perturbs the measured CARS signal that significantly distorts the spectral line shapes. It is an inherent limitation in all CARS-based methods. In this milieu, various optical-based techniques have been explored to tackle the NRB, such as single-Frequency CARS<sup>6</sup>, frequency modulation CARS<sup>7</sup>, polarization CARS<sup>8</sup>, interferometric CARS<sup>9</sup>, and pulse shaping CARS<sup>10</sup>. All these experimental methods have reduced the NRB contribution but at the cost of increasing experimental complexity and price. The NRB being a coherent signal, all these alternatives also drastically reduced the CARS spectral line intensities<sup>11</sup>, thus cancelling the benefit of the CARS approach<sup>12</sup>. Further, surrogate materials, such as coverslip-glass, salt, and water, have been traditionally utilized to reduce the NRB effect. These materials contain minimal or no vibrational peaks in a large spectroscopic window and have mitigated some of the ramifications but introduced errors in the measured amplitude.

Consequently, exploring for other methods to extract the phase relationship without physically removing the NRB is paramount. In this context, numerical approaches such as the maximum entropy method (MEM)<sup>13</sup> and the Kramers–Kronig (KK) relation<sup>14</sup> have been widely utilized for phase retrieval. Further, other algorithmic methods such as "phase-error correction"<sup>15</sup>, "factorized Kramers–Kronig and error correction"<sup>16</sup>, and "wavelet prism decomposition analysis"<sup>17</sup> also reported in the

<sup>a</sup> LUT School of Engineering Science, LUT University, 53851 Lappeenranta, Finland

<sup>b</sup> Leibniz Institute of Photonic Technology, Albert-Einstein-Strasse 9, 07745 Jena, Germany.

<sup>#</sup>Equal contribution

\* rajendhar.j2008@gmail.com

Electronic Supplementary Information (ESI) available: [details of any supplementary information available should be included here]. See DOI: 10.1039/x0xx00000x

## ARTICLE

## Journal Name

literature to mitigate the experimental artefacts and spectral line distortions in CARS spectra. Recently, Charles *et al.* proposed discrete Hilbert transform to remove the NRB<sup>18</sup>. However, these numerical techniques require surrogate reference material, and/or the other simulation parameters need to be tuned to get the best results. All these complications can be overcome by utilizing machine learning algorithms where the model learns from the input CARS data and predicts the Raman signal<sup>19</sup>. Deep neural networks (DNNs) have been explored in several applications, such as weather forecasting<sup>20</sup>, natural language processing<sup>21</sup>, and computer vision<sup>22</sup>. Moreover, it is also utilized in different spectroscopies, such as hyperspectral image analysis<sup>23</sup>, vibrational spectroscopy<sup>24,25</sup>, molecular excitation spectroscopy<sup>26</sup>, and laser-induced breakdown spectroscopy<sup>27–29</sup>.

Various deep learning (DL) approaches are also recently explored in CARS spectroscopy to tackle the NRB removal problem<sup>30–35</sup>. Valensise *et al.* have utilized a convolutional neural network (CNN) model to retrieve the imaginary part from CARS spectral data<sup>31</sup>. It is the first report on utilizing DL methods for removing the NRB and is referred to as SpecNet. Houhou *et al.* have used Long Short-Term Memory (LSTM) neural network model, to retrieve the Raman signal. Their results are then compared with the MEM & KK &<sup>30</sup>. Wang *et al.* deployed Very Deep Convolutional Autoencoders (VECTOR) for removing the NRB, and their model's performance is compared with SpecNet<sup>32</sup>. They have also shown that the VECTOR model with 16 layers has given optimum results in less computational time.

Our recent works demonstrated that retraining the SpecNet with a combination of semi-synthetic and synthetic data improves its performance<sup>33</sup>. We have also applied a transfer learning approach to increase the CNN model efficacy in retrieving the imaginary part of the CARS spectra<sup>34</sup>. Further, the noise is also varied at various levels to analyse the sensitivity of the model after transfer learning. Very recently, we have also explored three different NRB types to simulate the CARS data<sup>35</sup>. It has been revealed considering NRB as a fourth-order polynomial function instead of a product of two sigmoids improves the CNN model's efficiency. These three works have shown superior performance compared to the SpecNet, where spectral lines with minimal intensities are also predicted<sup>33–35</sup>. Even though the CNN model trained with polynomial NRB has predicted all the spectral lines of the experimental data but the intensity of a few lines deviated from the true one. Also, similar results were obtained with the LSTM<sup>30</sup> and VECTOR model<sup>32</sup>, where the performance was found to be sensitive when evaluating the experimental CARS data.

Further, estimating the mean square error (MSE) throughout the spectral range can be considered as a critical parameter for evaluating the model's efficiency. However, no other reports have presented it, excluding our works<sup>33–35</sup> to the best of our knowledge. It is noticed that the SpecNet has given high MSE while predicting the peaks at the ends of the spectrum. It is observed because the model could not be able to extract peaks

when it encountered the spectral line that only had a rising or falling part instead of a full line shape. Even retraining SpecNet with semi-synthetic data<sup>33</sup>, applying transfer learning<sup>34</sup>, and training with the CARS data simulated via polynomial NRB<sup>35</sup> could not avoid it and challenged the predictive ability of the models. These studies hint that exploring other DL approaches in addition to the CNN, LSTM, and VECTOR models can mitigate the aforementioned limitations.

Hence, in this work, we have explored the Bi-LSTM model for the first time for extracting the imaginary part of the CARS spectra. Also, the NRB is assumed as a fourth-order polynomial function while producing the CARS training data, which has already shown optimum results<sup>35</sup>. Further, a comprehensive study is performed by comparing the performance of four DL models viz, 1) VECTOR, 2) CNN, 3) LSTM, and 4) Bi-LSTM. This comparative study has been done for the first time to the best of our knowledge that critically evaluates the trained model's efficiency in retrieving the Raman signal from the CARS data.

## 2. Experimental details

### 2.1 CARS spectra simulation

All the models have been trained on pure synthetic spectral data with parameters of the number of peaks, intensity, frequency, and linewidths to enable it to be generalized to the different spectral shapes of NRBs. The CARS spectrum simulation procedure can be found in our previous work<sup>35</sup>. The simulation parameters details are presented in table 1.

Table 1. Details of the simulation parameters

S. No	Simulation parameters	Range
1	No of peaks	(1, 15)
2	Peak amplitude ( $A_k$ )	(0.01, 1)
3	Line width ( $\Gamma_k$ )	(0.001, 0.008)
4	Noise $\eta(\omega)$	(0.0005, 0.003)

In brief, the vibrational frequencies are sampled over a normalized scale [0, 1]. The NRB is considered as a function of fourth order polynomial as given in equation 2

$$NRB = a\omega^4 + b\omega^3 + c\omega^2 + d\omega + e \quad (2)$$

The coefficients  $a$ ,  $b$ , and  $d$  are randomly selected from the range of values [-10, 10], whereas it is [-1, 1] for  $c$  and  $e$  coefficients. The uniformly distributed noise  $\eta(\omega)$  is added to the chi3 data for generating CARS data. Total of 50000 synthetic training spectra are generated in Python, where each spectrum has 640 data points/wavenumbers. All the simulation parameters are randomly selected from the given range for generating each CARS spectrum, as shown in Table 1. The code to simulate the synthetic spectra is available here<sup>36</sup>. The synthetic dataset used for training all the models is the same (640 data points) except for the VECTOR, as its architecture inherently requires a longer data length (1000 data points). Hence 1D cubic spline interpolation was used to generate 1000 points from 640 points of the synthetic dataset. This technique

ensures that there will be no modifications in interpolation data concerning the shapes & intensity, as shown in Figure 1 in supplementary data.

## 2.2 Details of the experimental CARS data

The CARS data is acquired from the four samples, namely ADP, DMPC lipid, Yeast, and a protein droplet of FUS-LC (low-complexity domain of fused in sarcoma). The first three samples are recorded in one experimental configuration and its optical layout can be found here<sup>37</sup>. ADP is an equimolar mixture of AMP, ADP, and ATP in water with a total concentration of 500 mM. DMPC is small unilamellar vesicles (SUV) suspension with a concentration of 75 mM. The third sample is a living budding yeast cell (a zygote of *Saccharomyces cerevisiae*) measured from the mitochondria of the yeast cell<sup>38</sup>. An ultra-broadband CARS spectrum covering both the fingerprint and CH-vibration regions of FUS-LC droplet (protein) was measured by Y. Kan *et al* with a home-built broadband CARS microscope<sup>39</sup>. The protein sample is the low-complexity domain of RNA-binding protein fused in sarcoma (FUS-LC)<sup>39</sup>. Further, sample preparation details and the CARS measurements are explained elsewhere<sup>40</sup>. The CARS line-shape (the uppermost line-shape) was denoised by the Wavelet Prism procedure<sup>17</sup>, and the corresponding Raman line-shape was computed by the MEM procedure<sup>41</sup>.

## 3. Deep learning models

Four DL models, viz., 1) VECTOR, 2) CNN, 3) LSTM, and 4) Bi-LSTM details are briefly discussed in this section. The typical schematic of the fours model's architecture is presented in Figure 1 and the complete details are given in Table 1 in supplementary data. It is also worth considering that the Python code to train the VECTOR model is available in the GitHub repository but not the trained model weights<sup>42</sup>. So, we have directly retrained it by utilizing their code without modifying any of its model parameters. In the case of the CNN, the trained model weights are directly taken from our previous work<sup>35</sup> and can be accessed from here<sup>43</sup>. Houhou *et al.* have reported the LSTM model, but the trained weights and respective code is not openly available<sup>30</sup>. Therefore, we have retrained it without modifying the original model architecture. Finally, we have explored the Bi-LSTM model for the first time for CARS data analysis. The model architecture is inspired from this work<sup>44</sup>, where it was initially explored for analysing spectroscopic data of Type Ia Supernovae. However, we have modified the model parameters to achieve better results on the CARS data. All the trained model weights can be found in our GitHub repository<sup>36</sup>. All the computational details are given in Table 1 in supplementary data. Also, the model learning curves are visualized in Figure 4 in supplementary data

### 3.1 Convolutional neural networks (CNN)

The CNN architecture consists of convolutional and fully-connected layers together with pooling and flattening layers. The first part of the architecture includes a stack of convolution

layers extracting relevant features from the data and producing new data representations called "feature maps". The main advantage of convolutional layers is that they function as filter banks where the parameters are learned, and the level of abstraction related to the data representation increases layer-by-layer. Another benefit is moderate invariance to spatial or spectral translation enabled by the fact that each neuron in the convolution layer is connected to a limited neighbourhood of neurons of the preceding layer and the weights are shared by the neurons. This is relevant in Raman spectroscopy applications where the spectral lines/peaks can be shifted within the spectrum. In the second part of the architecture, fully-connected layers have no limitations concerning the connections from the preceding layer and their respective weights. They are used to learn the mapping from the feature representation to the desired output of a specific type and dimensionality.

The CNN architecture used here is SpecNet<sup>35</sup>. The typical schematic of the CNN model's architecture is presented in Figure 1(a). It is composed of five 1-dimension CLs (128,64,16,16,16) with filters of dimensions (32,16,8,8,8) and three FCLs of (32,16,640) dimensions, all followed by ReLU activation function while Adam is applied as the optimization function and the loss function is MSE. It aims to remove the NRB, which produces different levels of spectral distortions, from the input broadband CARS spectra.

### 3.2 Very deep convolutional autoencoders (VECTOR)

An autoencoder (AE) is an artificial neural network (ANN) architecture that encodes high-dimensional input data to a low-dimensional latent space and then learns how to reconstruct the input from this low-dimensional vector. This architecture has been applied to different problems including facial recognition<sup>45</sup>, feature detection<sup>46</sup>, and anomaly detection<sup>47</sup>. Typically, an AE is constructed from a symmetrical encoder and decoder with fully-connected layers<sup>48</sup>. The encoder receives high-dimensional input data, and during the training process learns how to reduce its dimension. It can be considered as a feature extractor that produces a feature representation of the lowest dimensionality from the encoder. In addition to reducing the dimensionality, this representation is unable to model the noise and nonessential information from the input data. The decoder learns how to reconstruct the input data from the encoded representation.

In this work, we have used the VECTOR-16 architecture proposed by Wang *et al.*<sup>32</sup>. We have retrained it by without modifying its architecture. It is composed of an eight layers encoder of fully convolutional (1D) and a symmetrical eight layers decoder of fully transposed convolutional (1D), and Stochastic gradient descent (SGD) was used as an optimizer. MAE is used as the loss function between the input CARS spectra and the clean Raman spectra. In addition, skip connections<sup>49</sup> been used that connect each layer from the encoder to the corresponding paired layer from the decoder

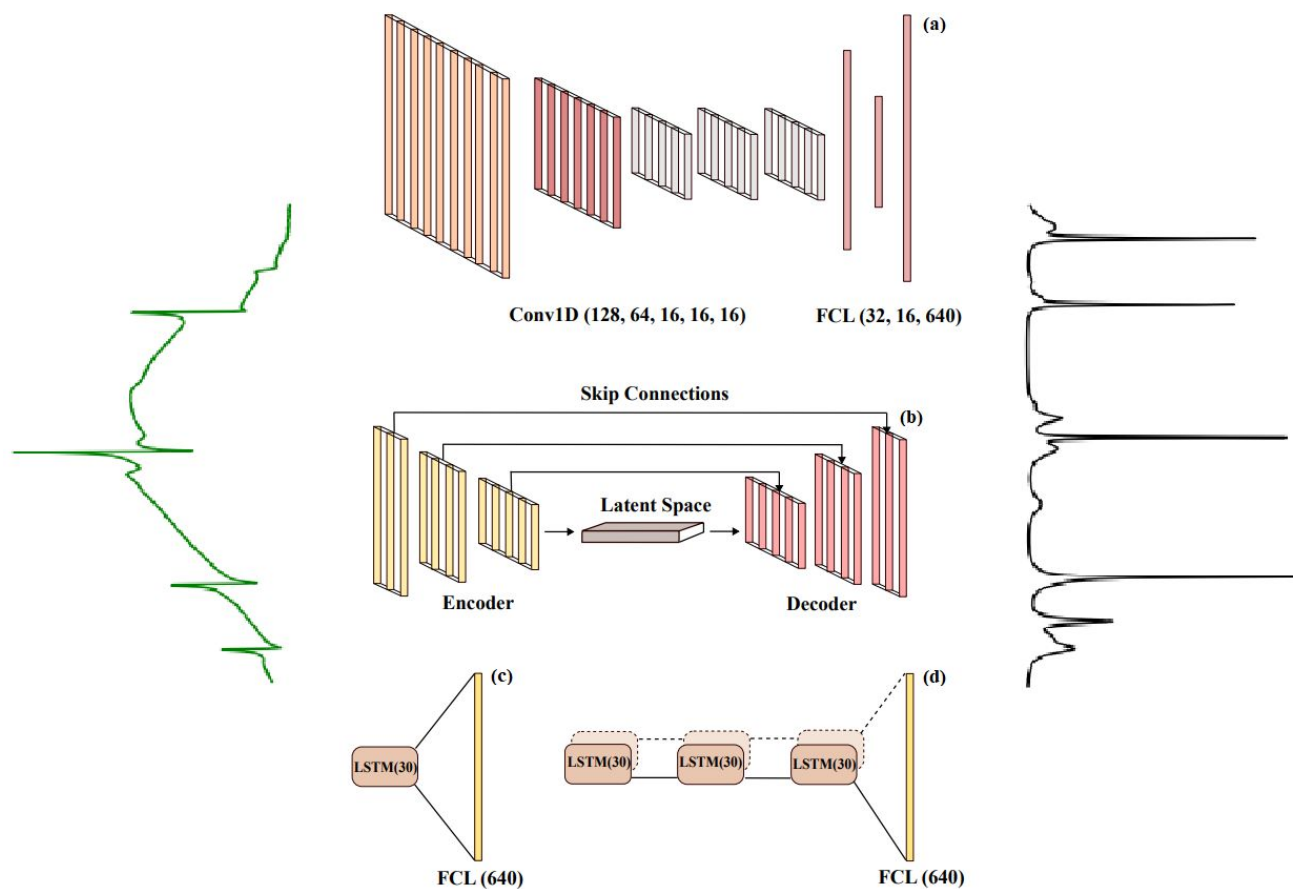


**Fig. 1** General schematic of the four models that are used including (a) convolutional neural network model, (b) autoencoder model, (cc) LSTM model and (d) Bi-LSTM model. The input for all four models is a CARS spectrum while the output is the corresponding Raman signal that is predicted by the models.

avoids the padding phenomenon that usually happens in convolutional layers. These skip connections speed up the training process and improve the model's performance in deeper networks compared to the plain ones. It also helps to mitigate the overfitting problem when the model is too complex and therefore improve the model generalization.

### 3.3 Long short-term memory (LSTM) neural network

A recurrent neural network (RNN) is a type of ANN that allows the modelling of temporal dynamic behaviour in the architecture by containing loops between the layers. This characteristic enables the data samples to be dependent on each other and memorization of previous information - a feature that traditional ANNs suffer from. However, RNNs suffer from a problem related to long-term dependencies, which means that if the delay/distance between the depending input samples or sequences increases, it cannot model such dependencies<sup>50</sup>. As a remedy for this problem, a long short-term memory (LSTM) network has been introduced<sup>51</sup>. The LSTM architecture is based upon four neural network layers, including the forget gate, input gate, output gate, and cell state.

The proposed LSTM architecture is adapted from this work<sup>30</sup>. Their code is not available for the direct reuse and its architecture is simple. It contains one LSTM layer of 30 units

with the ReLU as an activation function and Sigmoid as a recurrent activation function. The loss function is MSE, and the optimizer is Adam, while the learning rate is 0.005. They have simulated the CARS spectra with NRB as weak and strong regions.

### 3.4 Bi-Long short-term memory (Bi-LSTM) neural network

Bidirectional Long-Short Term Memory (Bi-LSTM)<sup>52</sup> network is a variant of the LSTM architecture that enables the input data sequence to be modelled in both directions, forward and backward. This is implemented by following the input sequence backward through an additional backward LSTM layer. Then the outputs of both forward and backward layers are combined through several ways including average, sum, multiplication, and concatenation. Using two LSTM layers improves the learning of the long-term dependencies and this leads to improved final accuracy of the model.

LSTM architecture is usually applied to ordered data without time labels like text classification or to constant time-sampling rate such as stock price predictions. All these are usually observed in irregular time-sampling rate. Hence a pre-processing method named functional principal component analysis (FPCA) was applied. Therefore, an additional dimension

is needed to contain the phase information of the spectrum. Hence the DL model should have an additional channel to contain it as the input data as well. LSTM does not have this channel so as the solution, the Bi-LSTM model has been used and the phase information was integrated as the input as well. The proposed Bi-LSTM architecture inspired from this work<sup>44</sup>. It consists of three bidirectional layers, each of them having 30 unit, and a time distributed fully connected layer as output, therefore, achieving an output for each time step. MSE and Nadam were used as the loss function and the optimizer respectively<sup>44</sup>.

## 4. Results and Discussion

In the following sections, the results of the four models are discussed. First, the models are evaluated on the simulated data and later experimentally measured CARS data.

### 4.1 Prediction on synthetic data

Initially, the efficiency of the four-trained models is demonstrated by retrieving the imaginary part from the 300 synthetic test spectra. These test spectra were independently generated apart from the training set where the spectral simulation parameter values are randomly selected from the given range of values as enumerated in table 1. The NRB utilized for generating training data is a 4<sup>th</sup> order polynomial function. However, three different NRBs were considered to simulate these 300 test spectra. Here, the idea is to estimate the four models' performance when they encounter the spectra simulated with NRB other than the 4<sup>th</sup> order polynomial function. Further, the first hundred spectra (1-100) of the 300 test spectra are simulated by considering the NRB as a 'Product of two Sigmoid', whereas spectra 101-200 are generated by assuming NRB as 'One sigmoid'. The last hundred (201-300) spectra were synthesized by adapting the NRB as a '4<sup>th</sup> order polynomial function'. These 300 synthetic test spectra are available here.<sup>43</sup>

#### 4.1.1 Extraction the imaginary part

Figure 2(a-d) represents the predicted imaginary part of the 295<sup>th</sup> test spectrum by the VECTOR, Bi-LSTM, CNN, and LSTM models, respectively. This spectrum is arbitrarily considered as an example from the entire test set only to visualize the efficacy of the four trained models. In each plot in the input CARS spectrum is presented at the top with green color. The true & predicted imaginary parts are shown in the middle, with black and green colors, respectively. The error between the true and predicted value is estimated then the square of the error (SE) is presented at the bottom with the blue line. This SE plot can be considered a visualization tool for validating the performance of the models. The four models extracted all the spectral lines, albeit their intensity has deviated from the actual one for some models, as shown in Figure 2(a-d). The estimated SE is found to be higher for LSTM, followed by the VECTOR, CNN, and Bi-LSTM, respectively.

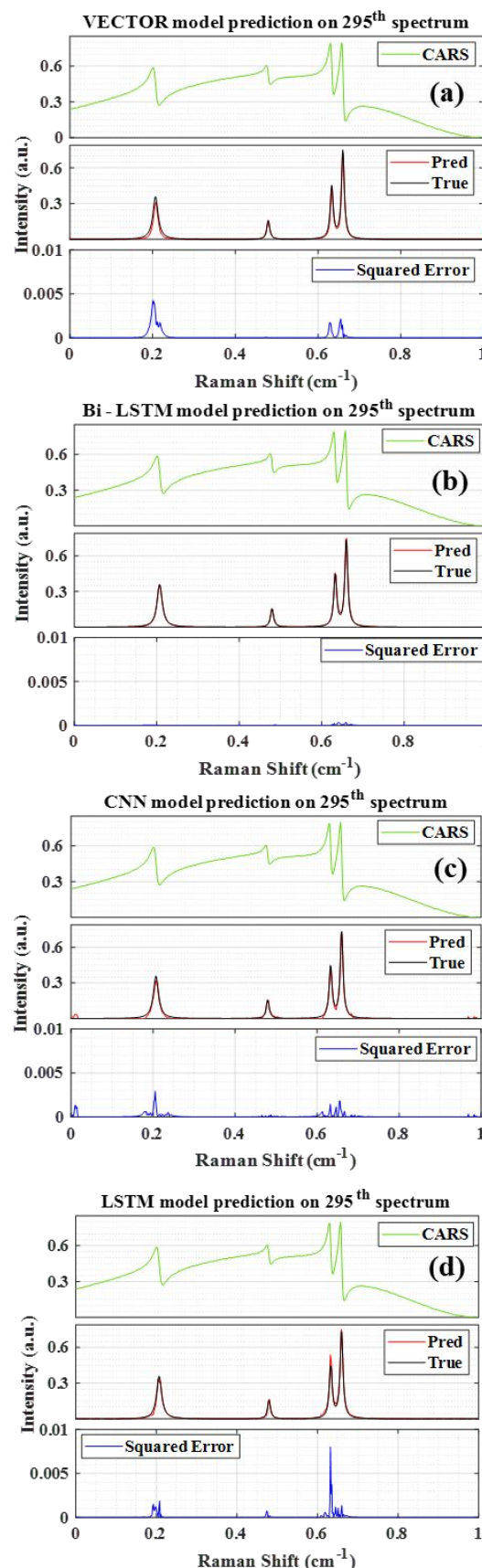


**Fig. 2** Comparison of the results obtained from the four models. a) VECTOR Prediction, b) Bi-LSTM Prediction, c) CNN Prediction, and d) LSTM Prediction. The labels 'True' & 'Pred' represent the true and predicted imaginary parts respectively.

## ARTICLE

## Journal Name

It is noticed that some peaks with lower intensity were observed on either side of the spectra for CNN, which were actually not present in the true Raman signal. These spurious lines can degrade the performance of the CNN compared to other models. In the case of LSTM, the predicted spectral line intensities are a little higher; on the contrary, it is slightly lower for the VECTOR prediction. Figure 2(c) illustrates the Raman signal retrieved from the Bi-LSTM model, where the extracted imaginary spectrum closely resembles the true spectrum. Also, it has not predicted any other spurious lines throughout the spectral range.

The SE plot visualization (represented at the bottom of the Figure, for example, see Figure 2a) efficaciously demonstrates the differences between the true and retrieved Raman signals throughout the spectral range for a single test spectrum. Nevertheless, visualization for the entire test set would not be feasible. Therefore, the mean square error (MSE) plot is considered for evaluating each trained model, as shown in Figure 3(a-d). The MSE is estimated by averaging the measured SE over 300 test spectra. The black dots in Figure 3(a-d) represent the average SE, and the red line corresponds to their standard deviation. For easy interpretation, the total spectral window can be divided into three parts first region ( $0\text{--}0.1\text{ cm}^{-1}$ ), mid-region ( $0.1\text{--}0.9\text{ cm}^{-1}$ ), and last region ( $0.6\text{--}1\text{ cm}^{-1}$ ), where the middle region itself accounts for 80 % of total data points, and the remaining 20 % represents first and last regions.

It is also observed that the error is less in the mid-region compared to the other two regions of the spectra. The measured MSE is highest in the first region compared to the remaining two regions, as shown in Figure 3(a-d). It is true for all four models, irrespective of their architecture. The standard deviation is found to be a maximum of  $\sim 0.06$  for the VECTOR and CNN, and it is slightly less for the LSTM  $\sim 0.055$ . However, a drastic change is observed in the case of the Bi-LSTM model, which has shown a 60 times lower standard deviation contrary to the other models, i.e., only  $\sim 0.0012$ . Also, the deviation is approximately the same throughout the spectral range except for a few points for the Bi-LSTM. However, the scenario is entirely different for the other three models. The deviation in the first region is more than 15 times compared to the mid-region for the VECTOR model, whereas it is 5 and 10 times for the LSTM and CNN models, respectively.

In the last region, the maximum deviation is observed for the CNN model, i.e.,  $\sim 0.035$ , whereas the minimum for the Bi-LSTM, i.e.,  $\sim 0.001$ . In the case of VECTOR, it is  $\sim 0.025$ , and it is  $\sim 0.005$  for the LSTM model. Also, the deviation is nearly the same in the mid and last regions for the LSTM. Overall, the MSE plot visually demonstrated that the Bi-LSTM model has a superior capability in predicting the imaginary part from the CARS spectra among all four models. The same behaviour is noticed for the mean absolute error (MAE) as shown in Figure 5 in supplementary data. In the following section, Pearson correlation analysis is performed. It provides a unique numerical parameter for each test spectrum, i.e., a correlation

coefficient. Hence, it can be utilized as a performance metric for validating the predictions of the four different models.

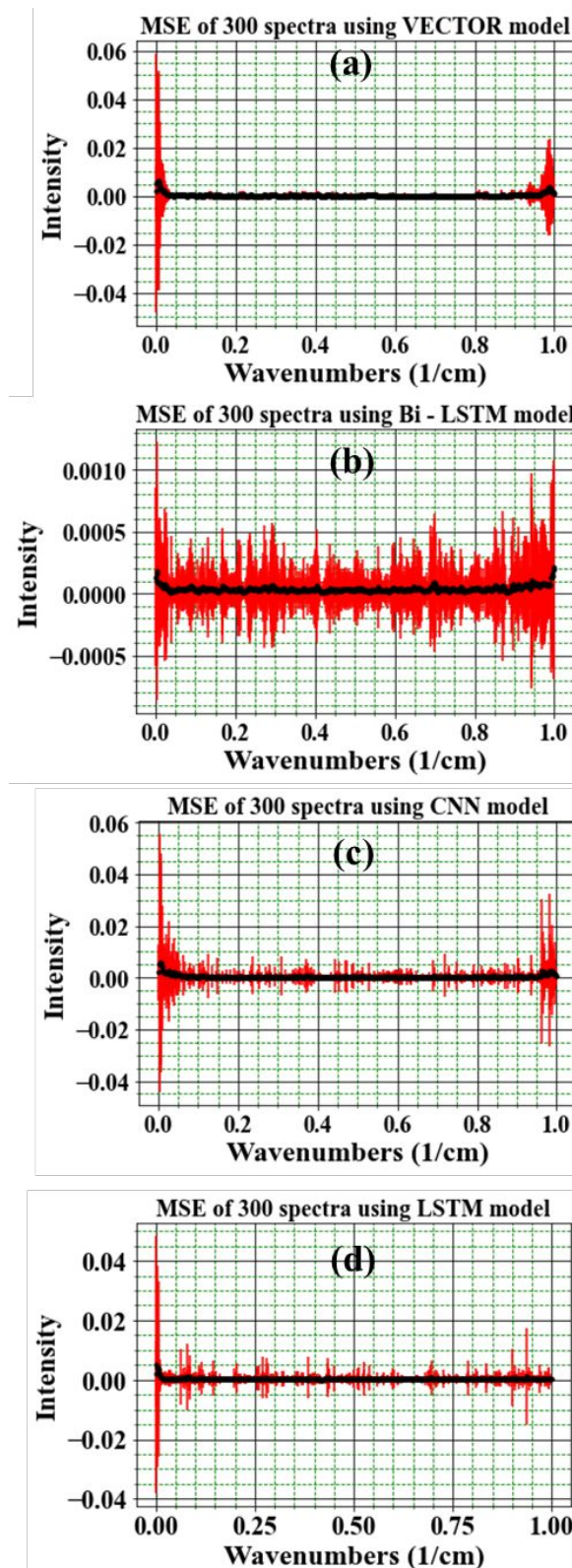


**Fig. 3 (a-d)** Represents the mean square error estimated for VECTOR, Bi-LSTM, CNN, and LSTM models, respectively. The black dots represent the mean value, whereas the red line corresponds to the standard deviation measured from the 300 test spectra.

#### 4.1.2 Pearson correlation analysis

It is a statistical approach that estimates the strength of the linear relationship between two sets of continuous variables and provides a unique numerical value, i.e., Pearson correlation coefficient (PCC)<sup>53</sup>. In this context, it represents a similarity percentage between the true and predicted imaginary parts of the CARS spectra. The measured PCC values can lie in the range of -1 and 1, which correspond to negative and positive linear correlation, respectively<sup>54</sup>. Overall, PCC value 1 represents the best match, i.e., true and predicted spectra are identical, whereas 0 corresponds to no similarity at all. Finally, the correlation analysis is performed on the imaginary parts predicted by the four models, and the results are presented in Figure 4(a-d), respectively. Two data points in the parathesis in Figure 4 represent the test spectrum number and its measured PCC value, respectively.

The PCC values estimated for the Bi-LSTM model have given higher coefficients compared to the other models for more than 97 % of test spectra, as shown in Figure 4(b).

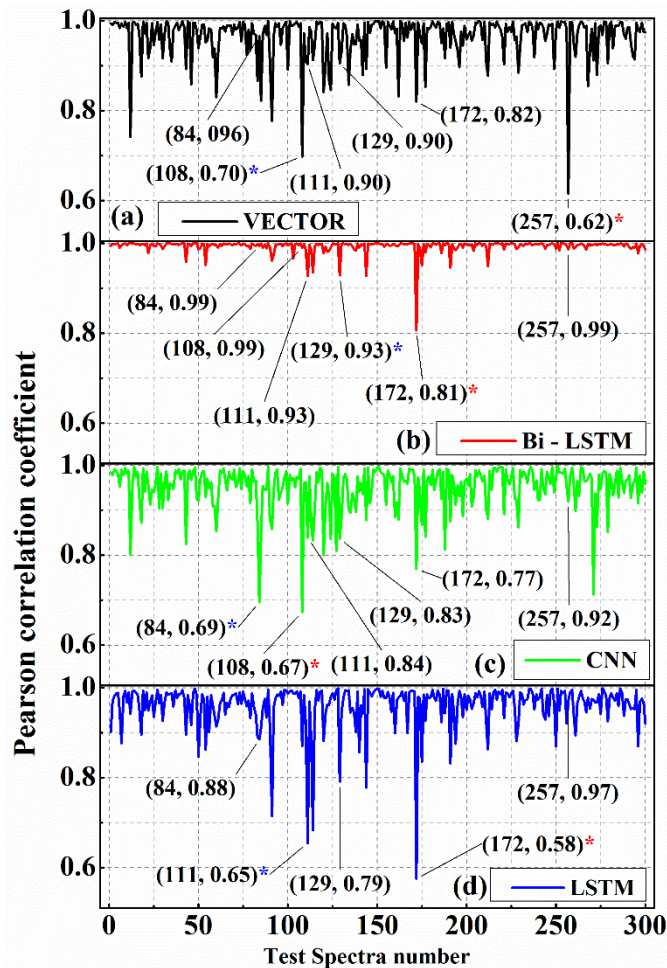


**Fig. 4** Pearson correlation coefficient (PCC) values estimated on predicted imaginary part by the a) VECTOR, b) LSTM, and c) CNN and d) LSTM models. The data points in the parenthesis represent the test spectrum number and its PCC value, respectively. A red asterisk denotes the lowest PCC value in the entire dataset. The blue asterisk represents the second-lowest PCC value.

Only one spectrum has given a PCC value of ~ 0.80 out of 300 spectra; all others have given PCCs of more than 0.92. In the case of CNN & VECTOR, four spectra have a PCC value less than 0.8, and it is five spectra for the LSTM model. Further, a histogram plot is drawn to graphically visualize the distribution of the estimated PCCs for the 300 test spectra, as shown in Figure 5. This plot presents the number of spectra that have the PCCs in a specific range, i.e., Frequency count in the selected PCC range. For example, seven spectra have PCC between 0.9-0.92 for the LSTM. Cumulatively, 273, 299, 264, and 273 spectra have PCCs > 0.9 for the VECTOR, Bi-LSTM, CNN, and LSTM models, respectively, which account for more than ~ 90 % of the test spectra. Hence, their distribution (on the x-axis) is presented only in the range of 0.9-1 instead of 0-1, which ascertains the best visualization of the PCCs distribution.

Also, it is noticed that 282 spectra have PCC values > 0.98 for the Bi-LSTM model, which corresponds to the ~ 94 % of total test data. It demonstrates that the Raman signal extracted using the Bi-LSTM model is in better agreement with the ground truth. On the other hand, only 102 and 131 spectra have PCC values > 0.98 for the CNN and LSTM models, respectively, which account for less than ~ 50 % of the total data. The CNN and LSTM models' performances were found to be almost the same when comparing their PCC values. Hence, the frequency count in most of the bins is approximately the same for the LSTM and CNN models. Further, their estimated PCCs difference is less than 0.05 for 253 spectra and less than 0.1 for 285 spectra, as shown in Figure 2 in supplementary data.

Further, it is observed that the maximum PCC value obtained is close to 1 for all the models. Nevertheless, the minimum values have shown a notable variation when compared with the predictions of the Bi-LSTM model. The lowest predicted PCC value is ~ 0.81 for the Bi-LSTM; meanwhile, it is ~ 0.58, ~ 0.62, and ~ 0.67 for the LSTM, VECTOR, and CNN models, respectively. The test spectrum with the lowest PCC value in each model is marked with a red asterisk (\*) for easy representation. For example, it is 257<sup>th</sup> spectrum for the VECTOR prediction, whereas it is 108<sup>th</sup> spectrum for CNN, and it is 172<sup>nd</sup> spectrum in the case of Bi-LSTM & LSTM models.

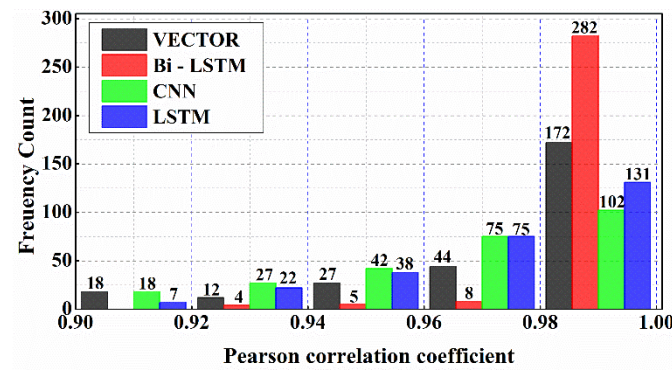


**Fig. 5** Histogram plot of the measured PCC values of the four models.

## ARTICLE

## Journal Name

The 2<sup>nd</sup> lowest PCC value is presented with a blue asterisk. These test spectra, along with their Raman line shapes extracted by the four models, are shown in Figure 6. These visualizations inherently represent the limitations of each model in retrieving the imaginary part from the CARS spectra. It also investigates the route cause for attaining the lowest PCC value for each trained model.

Figure 6(a1-a4) illustrates the results obtained from the 257<sup>th</sup> test spectrum using VECTOR, Bi-LSTM, CNN, and LSTM models, respectively. The input CARS spectrum has four spectral features in the entire spectral range where all the lines have higher intensity except for the peak at 0.66 cm<sup>-1</sup>. Among four lines, one is located near the right extrema, i.e., at 0.99 cm<sup>-1</sup>, and it could not be extracted by the VECTOR, whereas the other three models predicted it, but a huge error is found in the case of CNN. A similar observation was noticed in our previous work <sup>33</sup>, where the CNN prediction capability is poor at the edges. The LSTM and Bi-LSTM models have predicted all the lines, including the line at 0.99 cm<sup>-1</sup>, and the predictive performance was found to be the same for both models. Further, this inefficient extraction of the Raman line at 0.99 cm<sup>-1</sup> has given an SE of ~0.19 for the VECTOR and led to the minimum PCC value in the entire test dataset, i.e., ~0.62. The SE for the Bi-LSTM, LSTM, and CNN is ~0.005, ~0.01, and ~0.08, respectively.

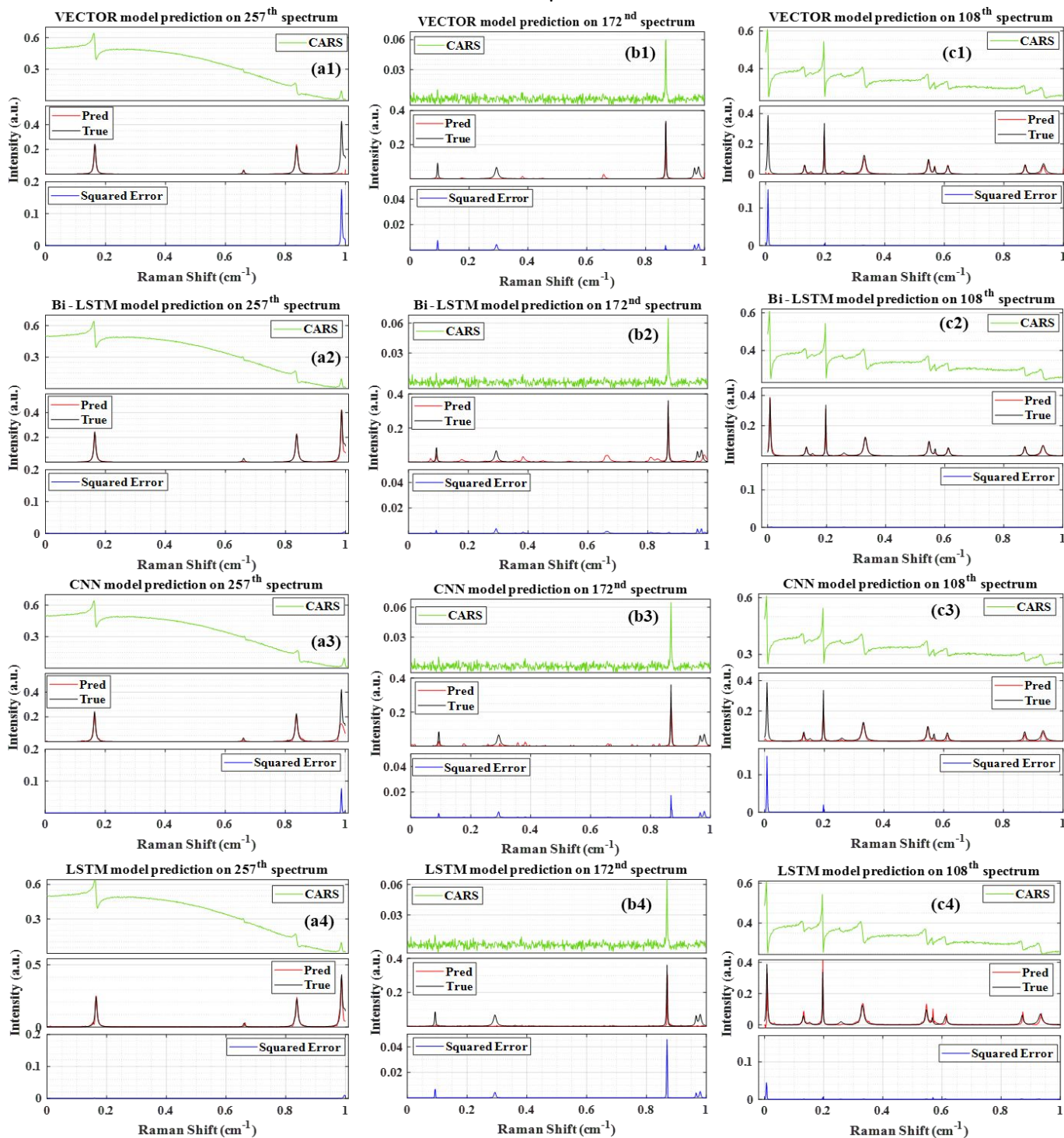
Figure 6(b1-b4) shows the results of the 172<sup>nd</sup> test spectrum obtained from the VECTOR, Bi-LSTM, CNN, and LSTM models, respectively. The input CARS spectrum has one strong line at ~0.86 cm<sup>-1</sup> and three very faint spectral lines in the remaining spectral range. These faint lines' intensities are close to the noise level. Also, the maximum spectral line intensity is only ~0.062, and due to this, the spectrum looks noisy compared to other test spectra where the intensities are higher by more than order. All four models predicted only one line at ~0.86 cm<sup>-1</sup>, and the rest of the lines were not extracted properly. Further, the predicted intensities are matched with the true one for the Bi-LSTM where the lowest SE is noticed, i.e., ~0.001, and the SE is 4, 48, and 18 times more for the VECTOR, LSTM, and CNN models, respectively. It is also observed that all the models have predicted some spurious lines with minute intensities throughout the spectral range. These observations affected the PCC measurements, and hence lowest coefficients, ~0.81 and ~0.58 are achieved for Bi-LSTM and LSTM models, respectively.

Figure 6(c1-c4) illustrates the 108<sup>th</sup> test spectrum results obtained from the VECTOR, Bi-LSTM, CNN, and LSTM models, respectively. The input CASRS spectrum has several vibrational spectral features with different peak intensities. Nevertheless, the first spectral line at ~0.006 cm<sup>-1</sup> (on the left extreme) has only half part, i.e., the spectral line is started with the trailing part instead of the rising part. It is observed due to considering the spectral line/peak generation anywhere on the entire spectral range (0-1) during the CARS spectra simulation. So, the lines generated close to the extremes sometimes have either a rising or trailing part depending on the peak position and width.

Hence, the error may also occur on the right side of the spectrum, as reported in our previous study <sup>33</sup>. The CNN and VECTOR models have predicted all the Raman lines except for the first line at ~0.006 cm<sup>-1</sup>, which is due to considering only half part of the spectral line. Similar observations were also noticed in the previous studies where the CNN model performance deteriorated when it encountered the spectral lines, with only having either a rising or trailing part <sup>33</sup>. This inherent constraint has given a high SE of ~0.15 and affected the PCC measurements, where its value is minimum (~0.67) for the CNN model and the second lowest PCC value (~0.70) for the VECTOR model. This could be a reason for the high MSE observed on either side of the extrema for the VECTOR and CNN models, as shown in Figure 3(a & c), respectively. Further, the Bi-LSTM and LSTM have predicted all the lines, including the first one on the left end. However, the LSTM model has given a high error compared to the Bi-LSTM model, which is of more than order.

Further, the test spectra corresponding to the second lowest PCC value are presented in supplementary Figure 3. It is the 84<sup>th</sup> spectrum for the CNN (~0.69) and 111<sup>th</sup> spectrum for the LSTM (~0.65), and 129<sup>th</sup> spectrum for the Bi-LSTM (~0.93) model. The results of the 111<sup>th</sup> spectrum are presented in supplementary Figure 3 (a1-a4), where the two spectral features are not predicted by the four models. These two spectral lines are very faint. Also, the predicted intestines have deviated, and the error is highest for the LSTM, which is reflected in PCC measurements, and the error is minimum for the Bi-LSTM. The results of the 129<sup>th</sup> test spectrum are shown in supplementary Figure 3(b1-b4), where the input CARS spectral lines intensity is low. The SE of the spectral line at ~0.97 (on the right extreme) is only ~0.004 for the Bi-LSTM, whereas it is more than 20 times for the other three models. However, the Bi-LSTM could not able to predict the two lines, which led to 2<sup>nd</sup> lowest PCC value. Further, the other three models also not retrieved three/four lines. In the case of the 84<sup>th</sup> spectrum, four models have predicted all the lines. Nevertheless, the retrieved peak intensities are deviated for all the models except for Bi-LSTM, as shown in supplementary Figure 3 (c1-c4). The deviation is found to be maximum for the CNN, followed by the LSTM, VECTOR, and Bi-LSTM, respectively. The SE of the spectral line at ~0.97 (on the right extreme) is only ~0.002 for the Bi-LSTM, whereas it is 30, 22, and 13 times more for the CNN, LSTM, and VECTOR models, respectively. These visual findings clearly demonstrate that the Bi-LSTM model has superior capability in predicting imaginary parts compared to the other three models.

In conclusion, Figures (4 & 6) and supplementary Figure 3 have visually demonstrated the imaginary part prediction capability of four models where the performance of the Bi-LSTM model was found to be best. Numerically, it performed well on more than 97 % of the total test dataset (i.e., it has a higher PCC value than the other three models). It also revealed that the Bi-LSTM model has better capability when extracting spectral lines at the ends, even though they only have either a rising or trailing part which led to the lowest MSE even at the edges, as shown in Figure 3(b).



**Fig. 6** Comparison of the results obtained from the four models. (a1-a2) Raman signal extracted from the 257<sup>th</sup> test spectra using VECTOR, Bi-LSTM, CNN, and LSTM models, respectively. (b1-b4) results of 172<sup>nd</sup> spectrum, (c1-c4) results of the 108<sup>th</sup> spectrum. ‘Pred’ is the predicted Raman signal, and ‘True’ represents the actual Raman signal. Squared error corresponds to their difference.

Further, the efficiency decreased when only it encountered the noisy CARS spectrum with very low intensity. The results of the experimental CARS spectra are discussed in detail in the next section.

#### 4.2 Prediction on experimental CARS spectra

This section critically examines the four trained model’s potential by retrieving the Raman signal from the experimentally recorded CARS spectra. This detailed interrogation provides a comprehensive overview of the

## ARTICLE

## Journal Name

model's performance when working with the real CARS data, viz., ADP/AMP/ATP mixture, DMPC, yeast, and protein samples. These biological samples have different resonance vibrational bands with various backgrounds. The sample preparation details and experimental setup overview is presented in section 2.2.

Figure 7 visualizes the results obtained from the four models on these experimental CARS data. Each plot in Figure 7 is a three-stacked plot (see Figure 7(a) for reference). The first row represents the input CARS spectrum (green line), and the second row visualizes the true (black line) and predicted (red line) imaginary parts. The labels 'True' and 'Pred' in the Figure correspond to the imaginary part extracted by the Maximum Entropy method and trained DL models, respectively. Further, the third row represents the square of the error (blue line), i.e., the square of the difference between the predicted and true imaginary parts. In each sample, the y-axis scale is considered to be the same for all four models for better visualization.

Figure 7(a1-a4) represents the results of the protein sample in the fingerprint region ( $700\text{--}1900\text{ cm}^{-1}$ ) obtained from the VECTOR, Bi-LSTM, CNN, and LSTM models, respectively. It has various resonance vibrational bands, including tyrosine peaks at 850, 1210, and  $1616\text{ cm}^{-1}$ , Amide I bands ( $\sim 1220\text{--}1250\text{ cm}^{-1}$ ), Amide III bands ( $\sim 1600\text{--}1700\text{ cm}^{-1}$ ), and CH<sub>2</sub> band at  $1445\text{ cm}^{-1}$ . Here the prediction of the Bi-LSTM model is in good agreement with the true one, where the SE is only  $\sim 0.02$ . In contrast, the LSTM model prediction is poor, where the extracted line shapes are very broad, and intensities deviate from the true ones. The other two models also predicted the spectral lines, albeit the intensities differed from the actual signal. Hence, the SE is found to be 6 times more for the VECTOR model compared to the Bi-LSTM, and it is 20 times for the LSTM and 5 times for the CNN. These observations are reflected in PCC measurements as shown in Figure 9(a), where the highest value is obtained for the Bi-LSTM, i.e.,  $\sim 0.95$ , and the minimum for the LSTM  $\sim 0.42$ . The other two have given the same value,  $\sim 0.89$ .

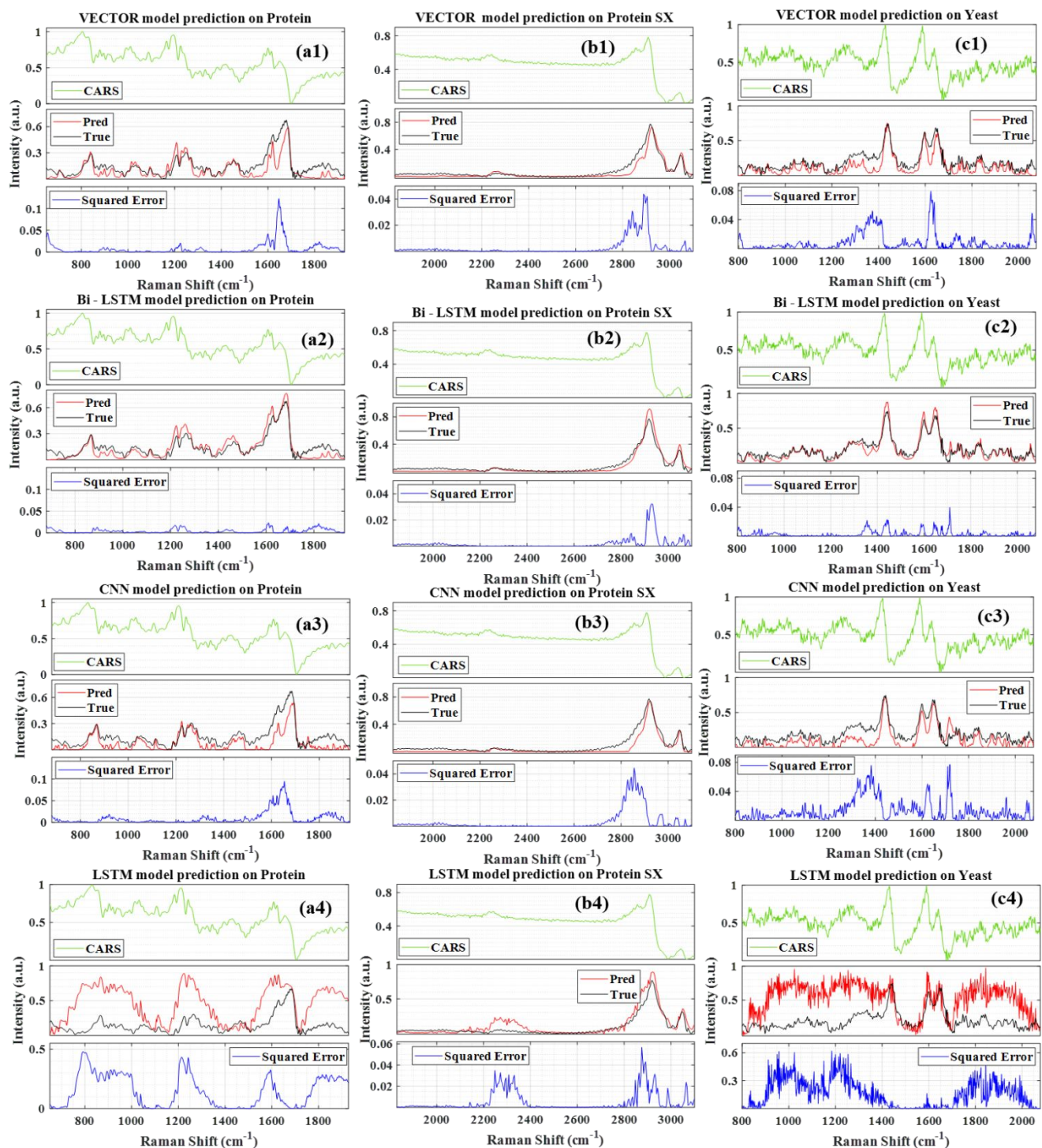
Figures 7(b1-b4) represent the results of the protein sample in the range of  $1830\text{--}3100\text{ cm}^{-1}$  from the VECTOR, Bi-LSTM, CNN, and LSTM models, respectively. The predicted line shapes are matching with true one for the Bi-LSTM, but the peak intensities have slightly deviated. On the contrary, the CNN and VECTOR models have correctly extracted the peak intensities; however, the line shapes have deteriorated. Similar behaviour is noticed for the LSTM, and in addition, a broad spurious peak is also observed in the spectral range of  $2200\text{--}2400\text{ cm}^{-1}$ . Overall minimum SE  $\sim 0.032$  is noticed for the Bi-LSTM and a maximum for the LSTM  $\sim 0.059$ .

Figure 7(c1-c4) illustrates the imaginary part retrieved from the yeast sample by these four models, respectively. All the models except for the LSTM have extracted major resonance spectral features (C-H bend of the aliphatic chain at  $1440\text{ cm}^{-1}$ , amide band at  $1654\text{ cm}^{-1}$ , C=C bending mode of phenylalanine at

$\sim 1590\text{ cm}^{-1}$ ); nonetheless, the predicted intensities have deviated for the VECTOR and CNN models compared to the Bi-LSTM. In the case of LSTM, an intense ringing structure has appeared throughout the spectral region, excluding resonance peak positions that are not present in the true Raman spectra. The maximum estimated SE for Bi-LSTM is  $\sim 0.04$ , and it is more than two times for the LSTM and CNN. The error is more than an order for the LSTM due to the deteriorated spectral line shapes. The measured PCC values also conveyed the same information where predictive performance is superior for the Bi-LSTM ( $\sim 0.96$ ) model followed by the VECTOR ( $\sim 0.92$ ), CNN ( $\sim 0.89$ ), and LSTM ( $\sim 0.41$ ) as shown in Figure 9(a).

The results of the ADP/AMP/ATP mixture obtained by the VECTOR, Bi-LSTM, and LSTM are presented in Figure 8 (a1-a3). The CNN model prediction can be found here<sup>35</sup>. The adenine vibrations are observed in the range of  $1270\text{--}1400\text{ cm}^{-1}$ , and the strongest one is noticed at  $\sim 1330\text{ cm}^{-1}$  as shown in Figure 8 (a1-a3)<sup>55</sup>. All four models have retrieved these adenine vibrations, albeit the extracted line intensities are not matching with the true intensities. The measured SE in this spectral range is noticed maximum for the VECTOR models ( $\sim 0.003$ ), followed by the LSMT ( $\sim 0.04$ ), Bi-LSTM ( $\sim 0.004$ ), and CNN ( $\sim 0.001$ )<sup>56</sup>. Further, the symmetric stretching vibration of the triphosphate group of ATP ( $\sim 1123\text{ cm}^{-1}$ ) is retrieved by all the models except for the LSTM. Hence the highest SE is observed for the LSTM ( $\sim 0.36$ ) and the minimum for the CNN ( $\sim 10^{-5}$ ). In the case of Bi-LSTM, the SE is  $\sim 10^{-4}$ , and it is  $\sim 10^{-2}$  for the VECTOR. Similar behaviour is noticed for the diphosphate resonance band ( $\sim 1100\text{ cm}^{-1}$ ). The monophosphate resonance band of AMP ( $979\text{ cm}^{-1}$ ) is only extracted by Bi-LSTM and CNN. The LSTM and VECTOR models could not able to predict it and led high SE. Here also, PCC values measured for all four models where the Bi-LSTM and CNN are the best among all as they have the highest coefficient  $\sim 0.93$ , followed by VECTOR ( $\sim 0.85$ ) and LSTM ( $\sim 0.42$ ).

Figure 8 (b1-b3) depicts the results of the DMPC sample retrieved from the VECTOR, Bi-LSTM, and LSTM models, respectively. The results of the CNN can be found here<sup>35</sup>. Prominent vibrational bands such as CH Strech mode, symmetric and antisymmetric stretching modes of methylene groups, and overtone of the methylene scissoring mode appeared in the range of  $2600\text{--}3000\text{ cm}^{-1}$ <sup>57,58</sup>. All four models have extracted these vibrational bands except for the LSTM. It could not able to predict the vibrational mode at  $2946\text{ cm}^{-1}$  and led to a high error. Also, a strong spurious line appeared on the right extreme for the LSTM prediction. These observations have affected the PCC measurements, where the PCCs values are  $\sim 0.8$ ,  $\sim 0.93$ ,  $\sim 0.89$ , and  $\sim 0.42$  for the VECTOR, Bi-LSTM, CNN, and LSTM models, respectively as shown in Figure 9(a). The Bi-LSTM model performance was found to be the best among all, where the highest average correlation coefficient is obtained for the Bi-LSTM, followed by CNN, VECTOR, and LSTM models, respectively, as shown in Figure 9(b). However, a relatively higher computational time is required for Bi-LSTM, as presented in Table 1 in supplementary data.



**Fig. 7** Results of the experimental CARS spectra. (a1-a4) the imaginary parts predicted by the VECTOR, Bi-LSTM, CNN, and LSTM models for the protein sample in the spectral range of 800–1800 cm<sup>-1</sup>, respectively. (b1-b4) prediction of the protein sample in the spectral range of 1830–3100 cm<sup>-1</sup>. (c1-c4) predictions on Yeast sample.

Overall, the BLSTM model predictions are optimum not only on the synthetic data but also on the experimental data. However, a few limitations were noticed when evaluating it on the spectra with low spectral line intensities and higher noise levels where it could not able to find some peaks. These observations suggest that modification of the spectral simulation parameters is required. Especially we are planning to train the model with

data generated by different noise levels in our future work. It would also be interesting to train the model with data generated by different simulation parameters (number of peaks, frequencies, amplitudes, etc.) to fit specific applications in different spectral regions<sup>59</sup>. Also, fine-tuning or transferring learning mechanisms can be explored to circumvent these limitations, which positively impacts model performance.

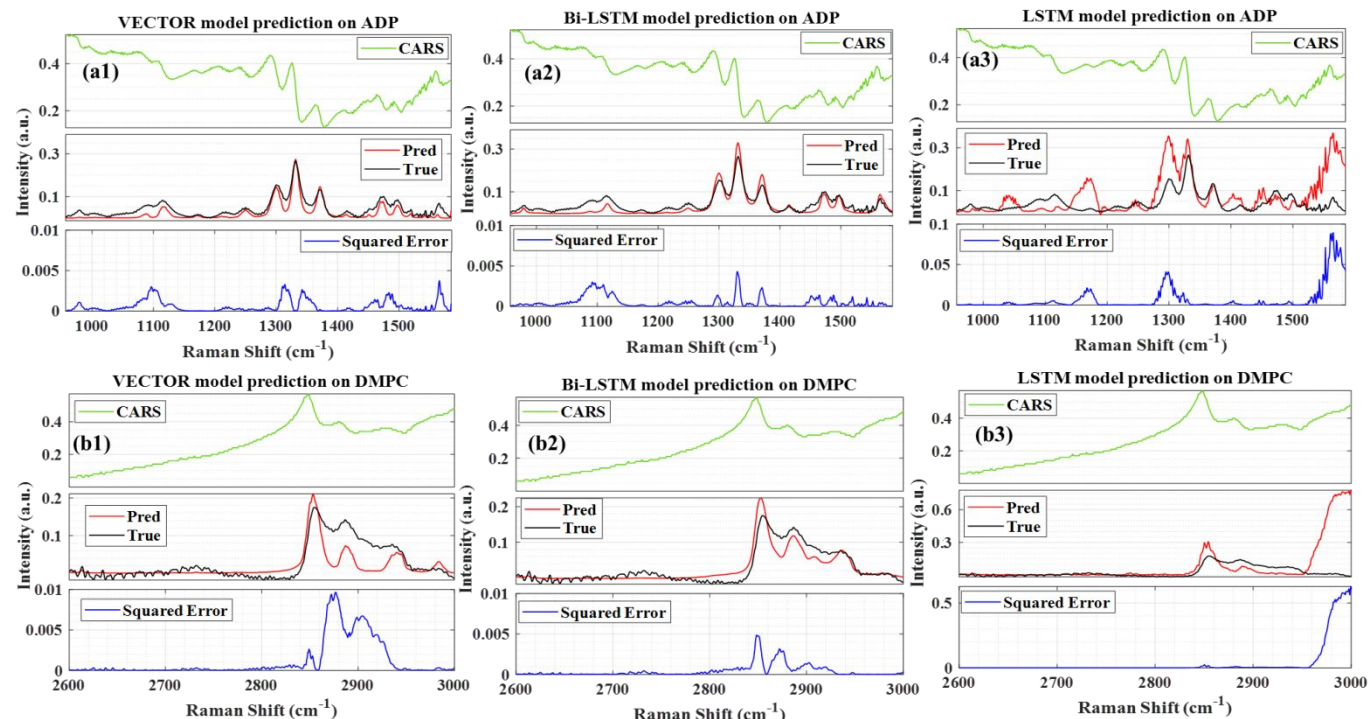


**Fig. 8** Results of the experimental CARS spectra. (a1-a3) the imaginary parts predicted by the VECTOR, Bi-LSTM and LSTM models for the ADP/AMP/ATP mixture, respectively. (b1-b3) predictions on DMPC sample.

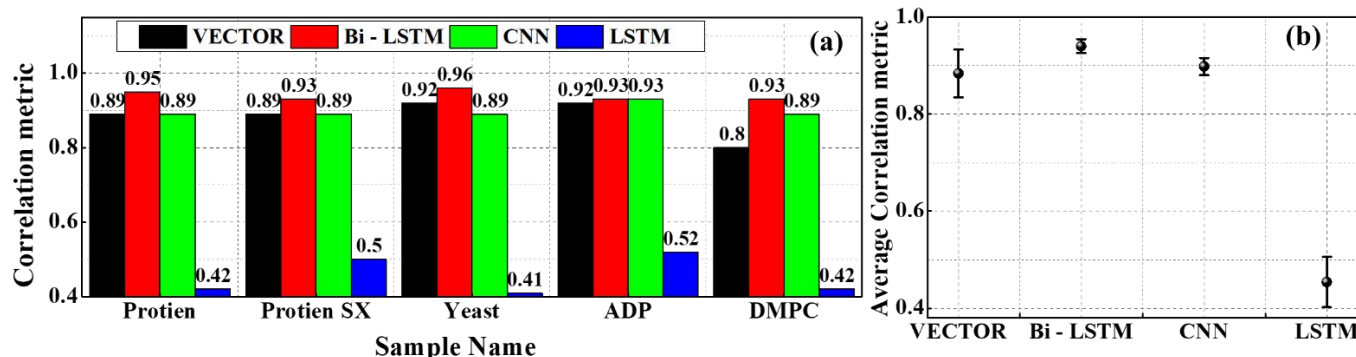


**Fig. 9** a) The PCCs values measured on the experimental CARS predictions using four trained models. b) The average value of the PCCs estimated from the five experimental CARS data.

## 5. Conclusions

We have systematically evaluated four DL models, namely CNN, LSTM, VECTOR, and Bi – LSTM, to retrieve the Raman signals from the CARS spectra. These four algorithms fundamentally differ from each other and provide a comprehensive overview in the context of applying them to CARS data analysis. All the models were trained with CARS simulated with the NRBs as a fourth-order polynomial function. The test dataset (300 spectra) is independently generated where three different NRBs (fourth-order polynomial function, product of two Sigmoid, and Single Sigmoid) are considered for every 100 spectra. The predictions of the test spectra revealed that Bi-

LSTM performance is superior, where the measured mean square error is 60 times less compared to the other three models. Also, it predicted the spectral lines on either end of the spectra, but the other three models could not able to extract the same. Further, the correlation analysis revealed that 97 % of test data has a higher correlation coefficient for the Bi-LSTM model than the other three models. Also, ~94 % of total test spectra have PCC values > 0.98 for the Bi-LSTM model, whereas 57 % for the VECTOR, 34 % for the LSTM, and 44 % for the CNN model. Finally, the predictions on four experimental samples (Protein, DMPC, ADP, and Yeast) also confirmed the same, where the predictive capability is best for the Bi-LSTM model compared to the other three. This systematic study shows that the Bi-LSTM model has great potential and provides a giant leap toward analysing the CARS data.

## Author Contributions

Rajendhar Junjuri (RJ), Lasse Lensu (LL), Erik M. Vartiainen (EMV) have conceived the idea of the experiment. Rajendhar Junjuri (RJ) has performed the analysis and prepared the initial Draft. Ali Saghi (AS), has trained VECTOR model and also contributed to the analysis part. Finally, the draft was revised by LL, EMV, and AS.

## Conflicts of interest

There are no conflicts to declare.

## Acknowledgements

This work is a part of the “Quantitative Chemically-Specific Imaging Infrastructure for Material and Life Sciences (qCSI)” project funded by the Academy of Finland (Grant No. FIRI/327734). Also, we thank Michiel Müller and Hilde Rinia for providing the experimental measurements of the DMPC lipid sample and the AMP/ADP/ATP mixture, as well as, Masanari Okuno and Hideaki Kano for providing the experimental measurements of the yeast sample and Yelena Kan and Sapun Parekh for providing the protein droplet measurements.

## References

- 1 A. Zumbusch, G. R. Holtom and X. S. Xie, Three-dimensional vibrational imaging by coherent anti-Stokes Raman scattering, *Phys. Rev. Lett.*, 1999, **82**, 4142.
- 2 L. M. Malard, L. Lafeta, R. S. Cunha, R. Nadas, A. Gadelha, L. G. Cançado and A. Jorio, Studying 2D materials with advanced Raman spectroscopy: CARS, SRS and TERS, *Phys. Chem. Chem. Phys.*, 2021, **23**, 23428–23444.
- 3 K. I. Popov, A. F. Pegoraro, A. Stolow and L. Ramunno, Image formation in CARS and SRS: effect of an inhomogeneous nonresonant background medium, *Opt. Lett.*, 2012, **37**, 473–475.
- 4 G. I. Petrov, R. Arora and V. V. Yakovlev, Coherent anti-Stokes Raman scattering imaging of microcalcifications associated with breast cancer, *Analyst*, 2021, **146**, 1253–1259.
- 5 C. L. Evans and X. S. Xie, Coherent anti-Stokes Raman scattering microscopy: chemical imaging for biology and medicine, *Annu. Rev. Anal. Chem.*, 2008, **1**, 883–909.
- 6 O. Burkacky, A. Zumbusch, C. Brackmann and A. Enejder, Dual-pump coherent anti-Stokes-Raman scattering microscopy, *Opt. Lett.*, 2006, **31**, 3656–3658.
- 7 F. Ganikhanov, C. L. Evans, B. G. Saar and X. S. Xie, High-sensitivity vibrational imaging with frequency modulation coherent anti-Stokes Raman scattering (FM CARS) microscopy, *Opt. Lett.*, 2006, **31**, 1872–1874.
- 8 J.-X. Cheng, L. D. Book and X. S. Xie, Polarization coherent anti-Stokes Raman scattering microscopy, *Opt. Lett.*, 2001, **26**, 1341–1343.
- 9 M. Jurna, J. P. Korterik, C. Otto, J. L. Herek and H. L. Offerhaus, Background free CARS imaging by phase sensitive heterodyne CARS, *Opt. Express*, 2008, **16**, 15863–15869.
- 10 S. O. Konorov, M. W. Blades and R. F. B. Turner, Lorentzian amplitude and phase pulse shaping for nonresonant background suppression and enhanced spectral resolution in coherent anti-Stokes Raman scattering spectroscopy and microscopy, *Appl. Spectrosc.*, 2010, **64**, 767–774.
- 11 M. Müller and A. Zumbusch, Coherent anti-Stokes Raman scattering microscopy, *ChemPhysChem*, 2007, **8**, 2156–2170.
- 12 M. Cui, B. R. Bachler and J. P. Ogilvie, Comparing coherent and spontaneous Raman scattering under biological imaging conditions, *Opt. Lett.*, 2009, **34**, 773–775.
- 13 E. M. Vartiainen, Phase retrieval approach for coherent anti-Stokes Raman scattering spectrum analysis, *JOSA B*, 1992, **9**, 1209–1214.
- 14 Y. Liu, Y. J. Lee and M. T. Cicerone, Broadband CARS spectral phase retrieval using a time-domain Kramers–Kronig transform, *Opt. Lett.*, 2009, **34**, 1363–1365.
- 15 C. H. Camp Jr, Y. J. Lee and M. T. Cicerone, Quantitative, comparable coherent anti-Stokes Raman scattering (CARS) spectroscopy: correcting errors in phase retrieval, *J. Raman Spectrosc.*, 2016, **47**, 408–415.
- 16 C. H. Camp Jr, J. S. Bender and Y. J. Lee, Real-time and high-throughput Raman signal extraction and processing in CARS hyperspectral imaging, *Opt. Express*, 2020, **28**, 20422–20437.
- 17 Y. Kan, L. Lensu, G. Hehl, A. Volkmer and E. M. Vartiainen, Wavelet prism decomposition analysis applied to CARS spectroscopy: a tool for accurate and quantitative extraction of resonant vibrational responses, *Opt. Express*, 2016, **24**, 11905–11916.
- 18 C. H. Camp, Raman signal extraction from CARS spectra using a learned-matrix representation of the discrete Hilbert transform, *Opt. Express*, 2022, **30**, 26057–26071.
- 19 Y. LeCun, Y. Bengio and G. Hinton, Deep learning, *Nature*, 2015, **521**, 436–444.
- 20 J. N. K. Liu, Y. Hu, Y. He, P. W. Chan and L. Lai, in *Information Granularity, Big Data, and Computational Intelligence*, Springer, 2015, pp. 389–408.
- 21 L. Deng and Y. Liu, *Deep learning in natural language processing*, Springer, 2018.
- 22 Y. Guo, Y. Liu, A. Oerlemans, S. Lao, S. Wu and M. S. Lew, Deep learning for visual understanding: A review, *Neurocomputing*, 2016, **187**, 27–48.
- 23 F. Lussier, V. Thibault, B. Charron, G. Q. Wallace and J.-F. Masson, Deep learning and artificial intelligence methods for Raman and surface-enhanced Raman scattering, *TrAC Trends Anal. Chem.*, 2020, **124**, 115796.
- 24 J. Yang, J. Xu, X. Zhang, C. Wu, T. Lin and Y. Ying, Deep learning for vibrational spectral analysis: Recent progress and a practical guide, *Anal. Chim. Acta*, 2019, **1081**, 6–17.
- 25 R. Luo, J. Popp and T. Bocklitz, Deep Learning for Raman Spectroscopy: A Review, *Analytica*, 2022, **3**, 287–301.
- 26 K. Ghosh, A. Stuke, M. Todorović, P. B. Jørgensen, M. N. Schmidt, A. Vehtari and P. Rinke, Deep learning

## ARTICLE

## Journal Name

- spectroscopy: Neural networks for molecular excitation spectra, *Adv. Sci.*, 2019, **6**, 1801367.
- 27 S. K. Anubham, R. Junjuri, A. K. Myakalwar and M. K. Gundawar, An approach to reduce the sample consumption for LIBS based identification of explosive materials, *Def. Sci. J.*, DOI:10.14429/dsj.67.10690.
- 28 E. Mal, R. Junjuri, M. K. Gundawar and A. Khare, Temporal characterization of laser-induced plasma of tungsten in air, *Laser Part. Beams*, 2020, **38**, 14–24.
- 29 R. Junjuri, S. A. Nalam, E. Manikanta, S. S. Harsha, P. P. Kiran and M. K. Gundawar, Spatio-temporal characterization of ablative Cu plasma produced by femtosecond filaments, *Opt. Express*, 2021, **29**, 10395.
- 30 R. Houhou, P. Barman, M. Schmitt, T. Meyer, J. Popp and T. Bocklitz, Deep learning as phase retrieval tool for CARS spectra, *Opt. Express*, 2020, **28**, 21002–21024.
- 31 C. M. Valensise, A. Giuseppi, F. Vernuccio, A. De la Cadena, G. Cerullo and D. Polli, Removing non-resonant background from CARS spectra via deep learning, *APL Photonics*, 2020, **5**, 61305.
- 32 Z. Wang, K. O' Dwyer, R. Muddiman, T. Ward, C. H. Camp and B. M. Hennelly, VECTOR: Very deep convolutional autoencoders for non-resonant background removal in broadband coherent anti-Stokes Raman scattering, *J. Raman Spectrosc.*, 2022, **53**, 1081–1093.
- 33 R. Junjuri, A. Saghi, L. Lensu and E. M. Vartiainen, Convolutional neural network-based retrieval of Raman signals from CARS spectra, *Opt. Contin.*, 2022, **1**, 1324.
- 34 A. Saghi, R. Junjuri, L. Lensu and E. Vartiainen, Semi-synthetic data generation to fine-tune a convolutional neural network for retrieving Raman signals from CARS spectra, *Opt. Contin.*, DOI:10.1364/OPTCON.469753.
- 35 R. Junjuri, A. Saghi, L. Lensu and E. M. Vartiainen, Effect of non-resonant background on the extraction of Raman signals from CARS spectra using deep neural networks, *RSC Adv.*, 2022, **12**, 28755–28766.
- 36 R. Junjuri, Four DL models evaluation on CARS data, <https://github.com/Junjuri/Four-DL-models-comparison-for-evaluating-CARS>.
- 37 M. Müller and J. M. Schins, Imaging the thermodynamic state of lipid membranes with multiplex CARS microscopy, *J. Phys. Chem. B*, 2002, **106**, 3715–3723.
- 38 M. Okuno, H. Kano, P. Leproux, V. Couderc, J. P. R. Day, M. Bonn and H. Hamaguchi, Quantitative CARS molecular fingerprinting of single living cells with the use of the maximum entropy method, *Angew. Chem. Int. Ed. Engl.*, 2010, **122**, 6925–6929.
- 39 A. C. Murthy, G. L. Dignon, Y. Kan, G. H. Zerze, S. H. Parekh, J. Mittal and N. L. Fawzi, Molecular interactions underlying liquid– liquid phase separation of the FUS low-complexity domain, *Nat. Struct. Mol. Biol.*, 2019, **26**, 637–648.
- 40 S. Chatterjee, Y. Kan, M. Brzezinski, K. Koynov, R. M. Regy, A. C. Murthy, K. A. Burke, J. J. Michels, J. Mittal and N. L. Fawzi, Reversible kinetic trapping of fus biomolecular condensates, *Adv. Sci.*, 2022, **9**, 2104247.
- 41 E. M. Vartiainen, H. A. Rinia, M. Müller and M. Bonn, Direct extraction of Raman line-shapes from congested CARS spectra, *Opt. Express*, 2006, **14**, 3622–3630.
- 42 VECTOR-CARS, <https://github.com/villawang/VECTOR-CARS>.
- 43 R. Junjuri, CARS data analysis with different NRB, <https://github.com/Junjuri/LUT>.
- 44 L. Hu, X. Chen and L. Wang, Spectroscopic Studies of Type Ia Supernovae Using LSTM Neural Networks, *Astrophys. J.*, 2022, **930**, 70.
- 45 G. E. Hinton, A. Krizhevsky and S. D. Wang, in *International conference on artificial neural networks*, Springer, 2011, pp. 44–51.
- 46 A. Géron, *Hands-on machine learning with Scikit-Learn, Keras, and TensorFlow*, 'O'Reilly Media, Inc.', 2022.
- 47 C.-Y. Liou, J.-C. Huang and W.-C. Yang, Modeling word perception using the Elman network, *Neurocomputing*, 2008, **71**, 3150–3157.
- 48 J. Schmidhuber, Deep learning in neural networks: An overview, *Neural networks*, 2015, **61**, 85–117.
- 49 K. He, X. Zhang, S. Ren and J. Sun, in *Proceedings of the IEEE conference on computer vision and pattern recognition*, 2016, pp. 770–778.
- 50 Z. C. Lipton, J. Berkowitz and C. Elkan, A critical review of recurrent neural networks for sequence learning, *arXiv Prepr. arXiv1506.00019*.
- 51 S. Hochreiter and J. Schmidhuber, Long short-term memory, *Neural Comput.*, 1997, **9**, 1735–1780.
- 52 M. Schuster and K. K. Paliwal, Bidirectional recurrent neural networks, *IEEE Trans. Signal Process.*, 1997, **45**, 2673–2681.
- 53 X. Tan, X. Chen and S. Song, A computational study of spectral matching algorithms for identifying Raman spectra of polycyclic aromatic hydrocarbons, *J. Raman Spectrosc.*, 2017, **48**, 113–118.
- 54 P. Schober, C. Boer and L. A. Schwarte, Correlation coefficients: appropriate use and interpretation, *Anesth. Analg.*, 2018, **126**, 1763–1768.
- 55 K. T. Yue, C. L. Martin, D. Chen, P. Nelson, D. L. Sloan and R. Callender, Raman spectroscopy of oxidized and reduced nicotinamide adenine dinucleotides, *Biochemistry*, 1986, **25**, 4941–4947.
- 56 L. Rimai, T. Cole, J. L. Parsons, J. T. Hickmott Jr and E. B. Carew, Studies of Raman spectra of water solutions of adenosine tri-, di-, and monophosphate and some related compounds, *Biophys. J.*, 1969, **9**, 320–329.
- 57 R. Mendelsohn and D. J. Moore, Vibrational spectroscopic studies of lipid domains in biomembranes and model systems, *Chem. Phys. Lipids*, 1998, **96**, 141–157.
- 58 A. Fasanella, K. Cosentino, A. Beneduci, G. Chidichimo, E. Cazzanelli, R. C. Barberi and M. Castriota, Thermal structural evolutions of DMPC-water biomimetic systems investigated by Raman Spectroscopy, *Biochim. Biophys. Acta (BBA)-Biomembranes*, 2018, **1860**, 1253–1258.
- 59 A. I. Cowen-Rivers, W. Lyu, R. Tutunov, Z. Wang, A. Grosnit, R. R. Griffiths, A. M. Maraval, H. Jianye, J. Wang and J. Peters, HEBO: Pushing The Limits of Sample-Efficient Hyper-parameter Optimisation, *J. Artif. Intell. Res.*, 2022, **74**, 1269–1349.



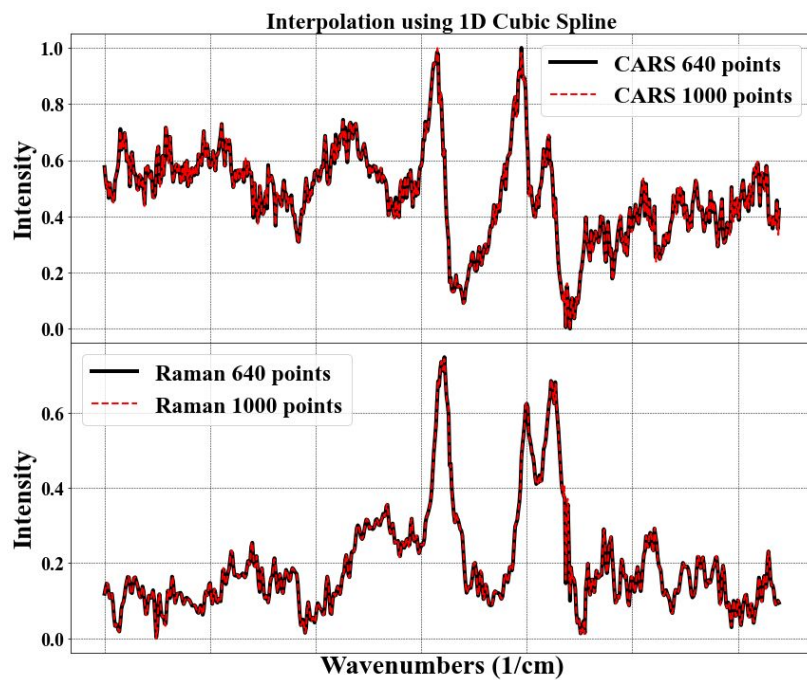
**Supplementary material**

Fig. 1 Interpolation of the CARS and Raman data. The data is interpolated to meet the length requirement of the VECTOR model.

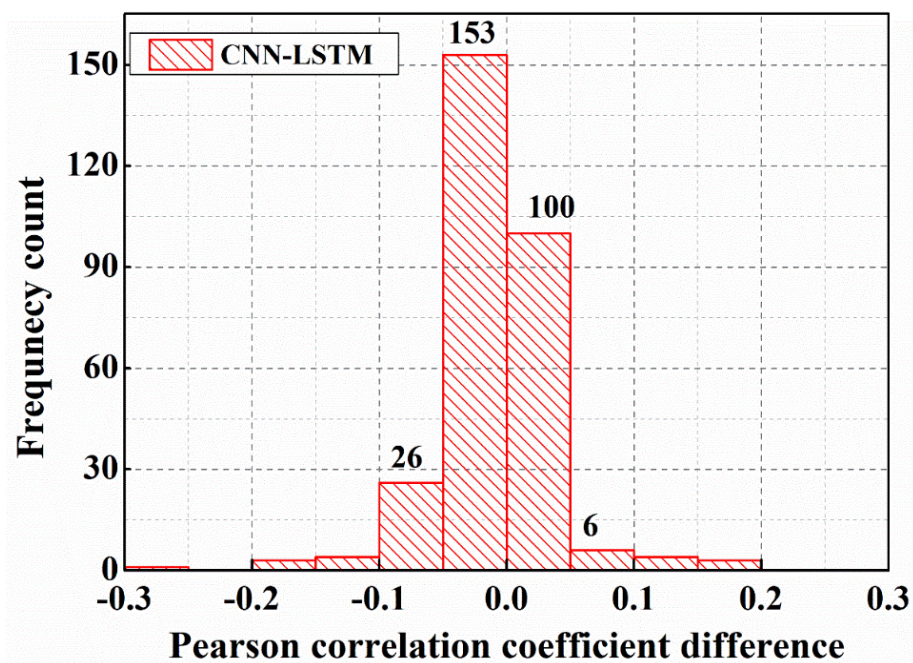
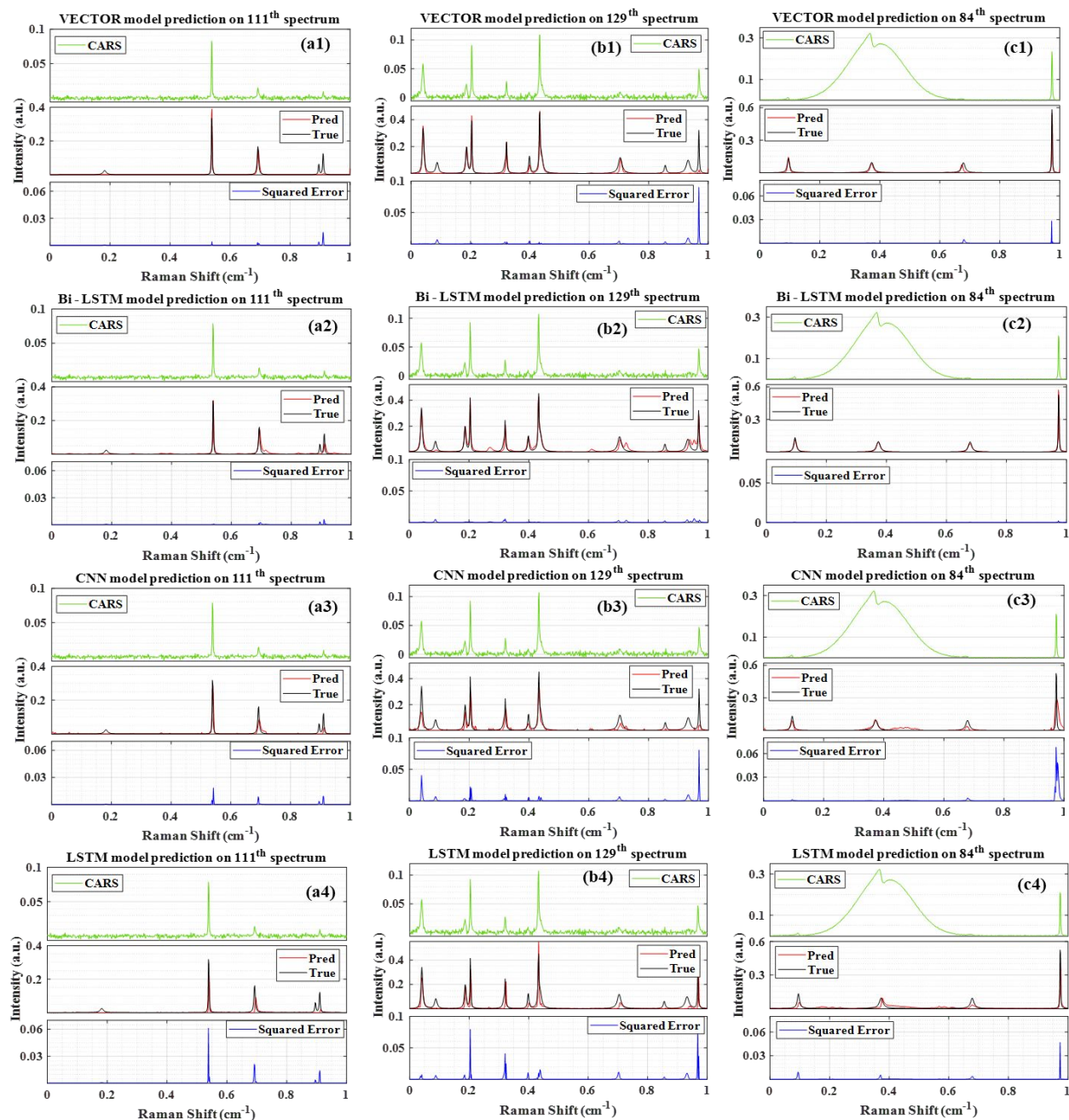


Fig. 2 Histogram plot of the PCC difference obtained from the CNN and LSTM model.



**Fig. 3** Histogram plot of the PCC difference obtained from the CNN and LSTM model. Comparison of the results obtained from the four models. (a1-a2) Raman signal extracted from the 111th test spectra using VECTOR, Bi-LSTM, CNN, and LSTM models respectively, (b1-b4) Results of 129<sup>th</sup> spectrum, (c1-c4) Results of the 84<sup>th</sup> spectrum. Pred is the predicted Raman signal, and True represents the actual Raman signal. Squared error corresponds to their difference.

### Computational times:

The key characteristics of the models were kept the same as in the original articles, and they are shown in Figure 1 in the manuscript. The models were trained and tested on a computer with an i5-11320H @ 3.20GHz, 12.0 GB RAM. The training times of the models differ significantly, as shown in below Table 1. Bi-LSTM and LSTM have long training times, although they contain much less parameters than the CNN and VECTOR models. In an LSTM architecture, each node is composed of 4 gates, including forget gate, input gate, output gate, and cell state, which all have their computation processes. Therefore, more calculations are needed in each node when compared with the regular ANN nodes. In a Bi-LSTM model, input data flows in both directions through

a bidirectional LSTM layer, so the computing time is increased. Also, the architecture contains an order of magnitude more parameters than the standard LSTM. In the case of VECTOR architecture, the large number of parameters in the encoders and decoders affect the training time. The inference times per sample are short, and the differences may be relevant in selected applications.

Table 1. Details of the computational parameters and times. Means square error (MSE) and mean absolute error (MAE) are loss functions. Stochastic gradient descent (SGD) is an optimizer for the VECTOR model.

S. No	Model	Loss Function	Optimizer	Parameters	Training time [h]	Testing time [ms]
1	CNN	MSE	Adam	6,016,932	0.8	77.1 ± 14.4
2	LSTM	MAE	Adam	3,871	5.6	83.7 ± 18.2
3	Bi-LSTM	MSE	Nadam	51,421	29.8	238.7 ± 22.5
4	VECTOR	MAE	SGD	178,942,720	12.6	51.6 ± 12.3

### Model learning curves:

The learning curves of the four deep learning models are shown in Figure 4. It should be noted that the magnitudes of the loss value in the plots are different. The training loss values are the batch loss averages within each epoch. In contrast, the validation loss values are the loss averages of the validation set using the current model. Therefore, in most cases, the validation loss is smaller than the training loss. To complement, dropout is used with the CNN and Bi-LSTM models affecting the training but not inference. The models' training processes converge differently. It is evident that with an appropriate criterion, early stopping of the training process could be adopted without affecting the model performance. This would also affect the training time, especially in the case of VECTOR, but also with the CNN and Bi-LSTM models.

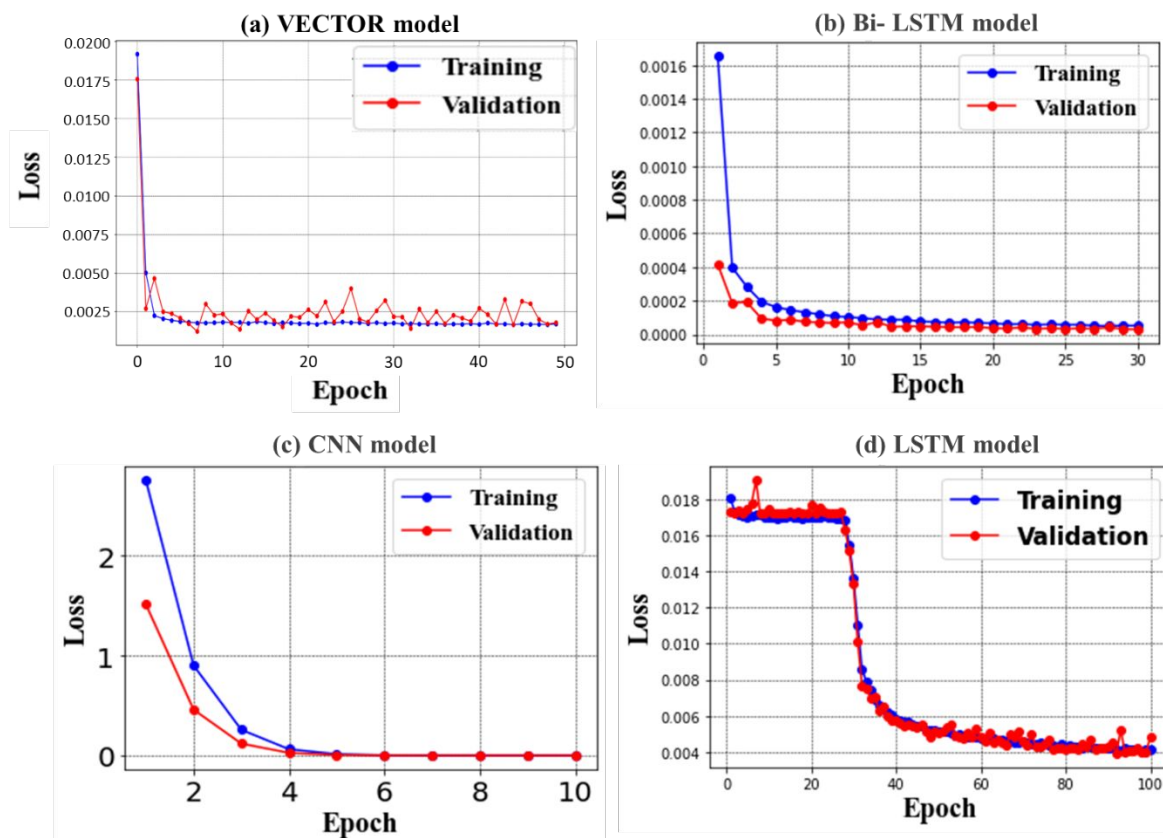


Fig. 4 (a-d) Represent the learning curves of VECTOR, Bi-LSTM, CNN, and LSTM models respectively.

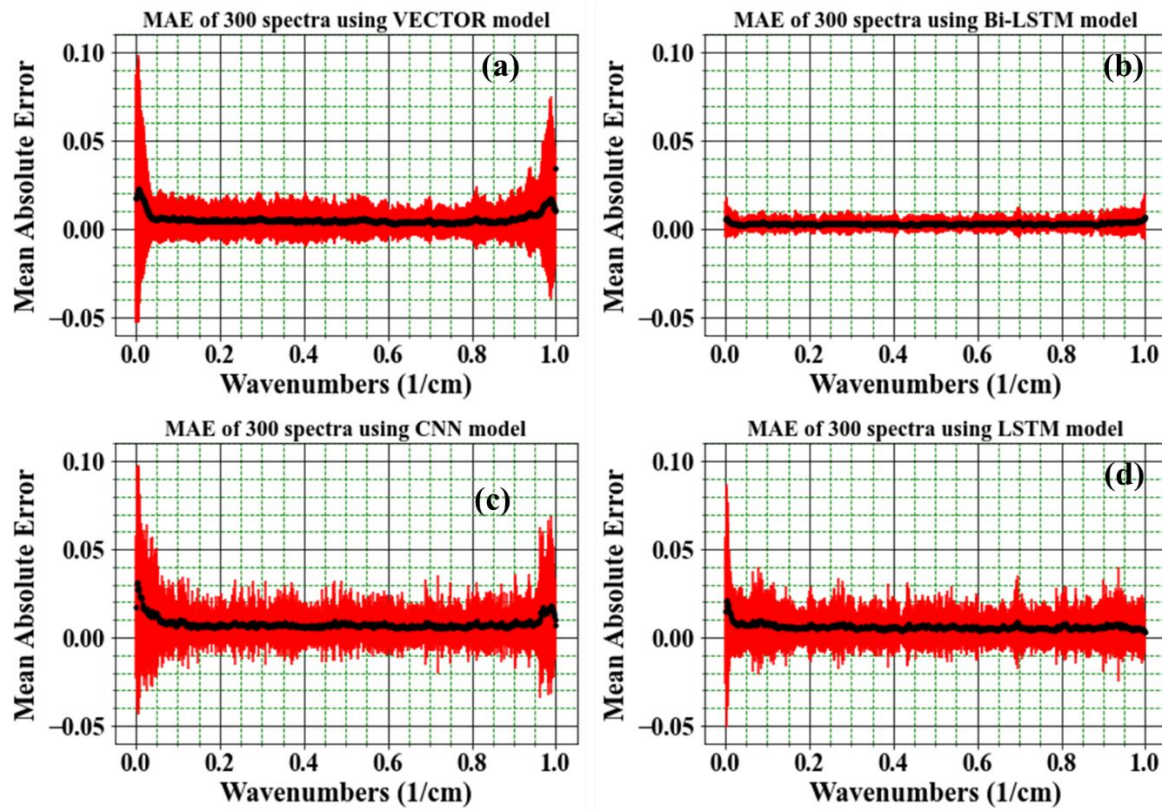


Fig 5. (a-d) Represent the mean absolute error (MAE) obtained from 300 test spectra for VECTOR, Bi-LSTM, CNN, and LSTM models respectively.

## ARTICLE

## Evaluating different deep learning models for efficient extraction of Raman signals from CARS spectra

Received 00th January 20xx,  
Accepted 00th January 20xx

DOI: 10.1039/x0xx00000x

Rajendhar Junjuri,<sup>a,b, #\*</sup> Ali Saghi <sup>#a</sup>, Lasse Lensu <sup>a</sup> and Erik M. Vartiainen <sup>a</sup>

The non-resonant background (NRB) contribution to the Coherent anti-Stokes Raman scattering (CARS) signal distorts the spectral line shapes and thus degrades the chemical information. Hence, finding an effective approach for removing NRB and extracting resonant vibrational signals is a challenging task. In this work, Bi-directional LSTM (Bi - LSTM) neural network is explored for the first time to remove NRB in CARS spectra automatically and, the results are compared with the three DL models reported in the literature viz, convolutional neural network (CNN), Long short-term memory (LSTM) neural network, very deep convolutional autoencoders (VECTOR). The results of the synthetic test data have shown that the Bi - LSTM model accurately extracts the spectral lines throughout the range. In contrast, the other three models' efficiency deteriorated while predicting the peaks on either end of the spectra, which resulted in a 60 times higher mean square error than the Bi - LSTM model. The Pearson correlation analysis demonstrated that Bi-LSTM model performance stands out from the rest, where 94 % of the test spectra have correlation coefficients of more than 0.99. Finally, these four models were evaluated on the four complex experimental CARS spectra viz, Protein, Yeast, DMPC, and ADP, where the Bi - LSTM model has shown superior performance, followed by CNN, VECTOR, and LSTM. This comprehensive study provides a giant leap toward simplifying the analysis of complex CARS spectroscopy and microscopy.

### 1. Introduction

The spontaneous Raman spectroscopic technique measures the vibrational response of molecules and provides functional and compositional information on the major chemical constituents. However, the acquired Raman signal strength is weak and, combined with the fluorescence contributions, results in longer acquisition times, limiting its applications. In contrast, Coherent anti-Stokes Raman scattering (CARS) is a nonlinear analytical method that offers similar fingerprint information to the spontaneous Raman technique, albeit orders of magnitude faster<sup>1,2</sup>. This characteristic property enabled it as a prominent spectroscopic tool for the label-free imaging of cells<sup>3</sup> and tissues<sup>4</sup> in biomedical applications<sup>5</sup>. Also, it has been significantly explored in other applications, such as materials science and nanotechnology. The intensity of the CARS signal is proportional to the susceptibility term and can be expressed as

$$I_{\text{CARS}} \propto |\chi_{\text{NR}}^{(3)} + \chi_R^{(3)}(\omega)|^2 \quad (1)$$

Here,  $\chi_{\text{NR}}^{(3)}$ ,  $\chi_R^{(3)}$  corresponds to the non-resonant and resonant third-order susceptibilities, respectively. As CARS being a coherent phenomenon the  $\chi_{\text{NR}}^{(3)}$ ,  $\chi_R^{(3)}$  responses of the sample

interfere via eq 1, and thus, the non-resonant background (NRB) contribution cannot be removed by simple subtraction. The NRB serves as a stable homodyne amplifier which is responsible for the signal strength of CARS. Nevertheless, this coherent contribution simultaneously perturbs the measured CARS signal that significantly distorts the spectral line shapes. It is an inherent limitation in all CARS-based methods. In this milieu, various optical-based techniques have been explored to tackle the NRB, such as single-Frequency CARS<sup>6</sup>, frequency modulation CARS<sup>7</sup>, polarization CARS<sup>8</sup>, interferometric CARS<sup>9</sup>, and pulse shaping CARS<sup>10</sup>. All these experimental methods have reduced the NRB contribution but at the cost of increasing experimental complexity and price. The NRB being a coherent signal, all these alternatives also drastically reduced the CARS spectral line intensities<sup>11</sup>, thus cancelling the benefit of the CARS approach<sup>12</sup>. Further, surrogate materials, such as coverslip-glass, salt, and water, have been traditionally utilized to reduce the NRB effect. These materials contain minimal or no vibrational peaks in a large spectroscopic window and have mitigated some of the ramifications but introduced errors in the measured amplitude.

Consequently, exploring for other methods to extract the phase relationship without physically removing the NRB is paramount. In this context, numerical approaches such as the maximum entropy method (MEM)<sup>13</sup> and the Kramers–Kronig (KK) relation<sup>14</sup> have been widely utilized for phase retrieval. Further, other algorithmic methods such as "phase-error correction"<sup>15</sup>, "factorized Kramers–Kronig and error correction"<sup>16</sup>, and "wavelet prism decomposition analysis"<sup>17</sup> also reported in the

<sup>a</sup> LUT School of Engineering Science, LUT University, 53851 Lappeenranta, Finland

<sup>b</sup> Leibniz Institute of Photonic Technology, Albert-Einstein-Strasse 9, 07745 Jena, Germany.

<sup>#</sup>Equal contribution

\* rajendhar.j2008@gmail.com

Electronic Supplementary Information (ESI) available: [details of any supplementary information available should be included here]. See DOI: 10.1039/x0xx00000x

## ARTICLE

## Journal Name

literature to mitigate the experimental artefacts and spectral line distortions in CARS spectra. Recently, Charles *et al.* proposed discrete Hilbert transform to remove the NRB<sup>18</sup>. However, these numerical techniques require surrogate reference material, and/or the other simulation parameters need to be tuned to get the best results. All these complications can be overcome by utilizing machine learning algorithms where the model learns from the input CARS data and predicts the Raman signal<sup>19</sup>. Deep neural networks (DNNs) have been explored in several applications, such as weather forecasting<sup>20</sup>, natural language processing<sup>21</sup>, and computer vision<sup>22</sup>. Moreover, it is also utilized in different spectroscopies, such as hyperspectral image analysis<sup>23</sup>, vibrational spectroscopy<sup>24,25</sup>, molecular excitation spectroscopy<sup>26</sup>, and laser-induced breakdown spectroscopy<sup>27–29</sup>.

Various deep learning (DL) approaches are also recently explored in CARS spectroscopy to tackle the NRB removal problem<sup>30–35</sup>. Valensise *et al.* have utilized a convolutional neural network (CNN) model to retrieve the imaginary part from CARS spectral data<sup>31</sup>. It is the first report on utilizing DL methods for removing the NRB and is referred to as SpecNet. Houhou *et al.* have used Long Short-Term Memory (LSTM) neural network model, to retrieve the Raman signal. Their results are then compared with the MEM & KK &<sup>30</sup>. Wang *et al.* deployed Very Deep Convolutional Autoencoders (VECTOR) for removing the NRB, and their model's performance is compared with SpecNet<sup>32</sup>. They have also shown that the VECTOR model with 16 layers has given optimum results in less computational time.

Our recent works demonstrated that retraining the SpecNet with a combination of semi-synthetic and synthetic data improves its performance<sup>33</sup>. We have also applied a transfer learning approach to increase the CNN model efficacy in retrieving the imaginary part of the CARS spectra<sup>34</sup>. Further, the noise is also varied at various levels to analyse the sensitivity of the model after transfer learning. Very recently, we have also explored three different NRB types to simulate the CARS data<sup>35</sup>. It has been revealed considering NRB as a fourth-order polynomial function instead of a product of two sigmoids improves the CNN model's efficiency. These three works have shown superior performance compared to the SpecNet, where spectral lines with minimal intensities are also predicted<sup>33–35</sup>. Even though the CNN model trained with polynomial NRB has predicted all the spectral lines of the experimental data but the intensity of a few lines deviated from the true one. Also, similar results were obtained with the LSTM<sup>30</sup> and VECTOR model<sup>32</sup>, where the performance was found to be sensitive when evaluating the experimental CARS data.

Further, estimating the mean square error (MSE) throughout the spectral range can be considered as a critical parameter for evaluating the model's efficiency. However, no other reports have presented it, excluding our works<sup>33–35</sup> to the best of our knowledge. It is noticed that the SpecNet has given high MSE while predicting the peaks at the ends of the spectrum. It is observed because the model could not be able to extract peaks

when it encountered the spectral line that only had a rising or falling part instead of a full line shape. Even retraining SpecNet with semi-synthetic data<sup>33</sup>, applying transfer learning<sup>34</sup>, and training with the CARS data simulated via polynomial NRB<sup>35</sup> could not avoid it and challenged the predictive ability of the models. These studies hint that exploring other DL approaches in addition to the CNN, LSTM, and VECTOR models can mitigate the aforementioned limitations.

Hence, in this work, we have explored the Bi-LSTM model for the first time for extracting the imaginary part of the CARS spectra. Also, the NRB is assumed as a fourth-order polynomial function while producing the CARS training data, which has already shown optimum results<sup>35</sup>. Further, a comprehensive study is performed by comparing the performance of four DL models viz, 1) VECTOR, 2) CNN, 3) LSTM, and 4) Bi-LSTM. This comparative study has been done for the first time to the best of our knowledge that critically evaluates the trained model's efficiency in retrieving the Raman signal from the CARS data.

## 2. Experimental details

### 2.1 CARS spectra simulation

All the models have been trained on pure synthetic spectral data with parameters of the number of peaks, intensity, frequency, and linewidths to enable it to be generalized to the different spectral shapes of NRBs. The CARS spectrum simulation procedure can be found in our previous work<sup>35</sup>. The simulation parameters details are presented in table 1.

Table 1. Details of the simulation parameters

S. No	Simulation parameters	Range
1	No of peaks	(1, 15)
2	Peak amplitude ( $A_k$ )	(0.01, 1)
3	Line width ( $\Gamma_k$ )	(0.001, 0.008)
4	Noise $\eta(\omega)$	(0.0005, 0.003)

In brief, the vibrational frequencies are sampled over a normalized scale [0, 1]. The NRB is considered as a function of fourth order polynomial as given in equation 2

$$NRB = a\omega^4 + b\omega^3 + c\omega^2 + d\omega + e \quad (2)$$

The coefficients  $a$ ,  $b$ , and  $d$  are randomly selected from the range of values [-10, 10], whereas it is [-1, 1] for  $c$  and  $e$  coefficients. The uniformly distributed noise  $\eta(\omega)$  is added to the chi3 data for generating CARS data. Total of 50000 synthetic training spectra are generated in Python, where each spectrum has 640 data points/wavenumbers. All the simulation parameters are randomly selected from the given range for generating each CARS spectrum, as shown in Table 1. The code to simulate the synthetic spectra is available here<sup>36</sup>. The synthetic dataset used for training all the models is the same (640 data points) except for the VECTOR, as its architecture inherently requires a longer data length (1000 data points). Hence 1D cubic spline interpolation was used to generate 1000 points from 640 points of the synthetic dataset. This technique

ensures that there will be no modifications in interpolation data concerning the shapes & intensity, as shown in Figure 1 in supplementary data.

## 2.2 Details of the experimental CARS data

The CARS data is acquired from the four samples, namely ADP, DMPC lipid, Yeast, and a protein droplet of FUS-LC (low-complexity domain of fused in sarcoma). The first three samples are recorded in one experimental configuration and its optical layout can be found here<sup>37</sup>. ADP is an equimolar mixture of AMP, ADP, and ATP in water with a total concentration of 500 mM. DMPC is small unilamellar vesicles (SUV) suspension with a concentration of 75 mM. The third sample is a living budding yeast cell (a zygote of *Saccharomyces cerevisiae*) measured from the mitochondria of the yeast cell<sup>38</sup>. An ultra-broadband CARS spectrum covering both the fingerprint and CH-vibration regions of FUS-LC droplet (protein) was measured by Y. Kan *et al* with a home-built broadband CARS microscope<sup>39</sup>. The protein sample is the low-complexity domain of RNA-binding protein fused in sarcoma (FUS-LC)<sup>39</sup>. Further, sample preparation details and the CARS measurements are explained elsewhere<sup>40</sup>. The CARS line-shape (the uppermost line-shape) was denoised by the Wavelet Prism procedure<sup>17</sup>, and the corresponding Raman line-shape was computed by the MEM procedure<sup>41</sup>.

## 3. Deep learning models

Four DL models, viz., 1) VECTOR, 2) CNN, 3) LSTM, and 4) Bi-LSTM details are briefly discussed in this section. The typical schematic of the fours model's architecture is presented in Figure 1 and the complete details are given in Table 1 in supplementary data. It is also worth considering that the Python code to train the VECTOR model is available in the GitHub repository but not the trained model weights<sup>42</sup>. So, we have directly retrained it by utilizing their code without modifying any of its model parameters. In the case of the CNN, the trained model weights are directly taken from our previous work<sup>35</sup> and can be accessed from here<sup>43</sup>. Houhou *et al.* have reported the LSTM model, but the trained weights and respective code is not openly available<sup>30</sup>. Therefore, we have retrained it without modifying the original model architecture. Finally, we have explored the Bi-LSTM model for the first time for CARS data analysis. The model architecture is inspired from this work<sup>44</sup>, where it was initially explored for analysing spectroscopic data of Type Ia Supernovae. However, we have modified the model parameters to achieve better results on the CARS data. All the trained model weights can be found in our GitHub repository<sup>36</sup>. All the computational details are given in Table 1 in supplementary data. Also, the model learning curves are visualized in Figure 4 in supplementary data

### 3.1 Convolutional neural networks (CNN)

The CNN architecture consists of convolutional and fully-connected layers together with pooling and flattening layers. The first part of the architecture includes a stack of convolution

layers extracting relevant features from the data and producing new data representations called "feature maps". The main advantage of convolutional layers is that they function as filter banks where the parameters are learned, and the level of abstraction related to the data representation increases layer-by-layer. Another benefit is moderate invariance to spatial or spectral translation enabled by the fact that each neuron in the convolution layer is connected to a limited neighbourhood of neurons of the preceding layer and the weights are shared by the neurons. This is relevant in Raman spectroscopy applications where the spectral lines/peaks can be shifted within the spectrum. In the second part of the architecture, fully-connected layers have no limitations concerning the connections from the preceding layer and their respective weights. They are used to learn the mapping from the feature representation to the desired output of a specific type and dimensionality.

The CNN architecture used here is SpecNet<sup>35</sup>. The typical schematic of the CNN model's architecture is presented in Figure 1(a). It is composed of five 1-dimension CLs (128,64,16,16,16) with filters of dimensions (32,16,8,8,8) and three FCLs of (32,16,640) dimensions, all followed by ReLU activation function while Adam is applied as the optimization function and the loss function is MSE. It aims to remove the NRB, which produces different levels of spectral distortions, from the input broadband CARS spectra.

### 3.2 Very deep convolutional autoencoders (VECTOR)

An autoencoder (AE) is an artificial neural network (ANN) architecture that encodes high-dimensional input data to a low-dimensional latent space and then learns how to reconstruct the input from this low-dimensional vector. This architecture has been applied to different problems including facial recognition<sup>45</sup>, feature detection<sup>46</sup>, and anomaly detection<sup>47</sup>. Typically, an AE is constructed from a symmetrical encoder and decoder with fully-connected layers<sup>48</sup>. The encoder receives high-dimensional input data, and during the training process learns how to reduce its dimension. It can be considered as a feature extractor that produces a feature representation of the lowest dimensionality from the encoder. In addition to reducing the dimensionality, this representation is unable to model the noise and nonessential information from the input data. The decoder learns how to reconstruct the input data from the encoded representation.

In this work, we have used the VECTOR-16 architecture proposed by Wang *et al.*<sup>32</sup>. We have retrained it by without modifying its architecture. It is composed of an eight layers encoder of fully convolutional (1D) and a symmetrical eight layers decoder of fully transposed convolutional (1D), and Stochastic gradient descent (SGD) was used as an optimizer. MAE is used as the loss function between the input CARS spectra and the clean Raman spectra. In addition, skip connections<sup>49</sup> been used that connect each layer from the encoder to the corresponding paired layer from the decoder

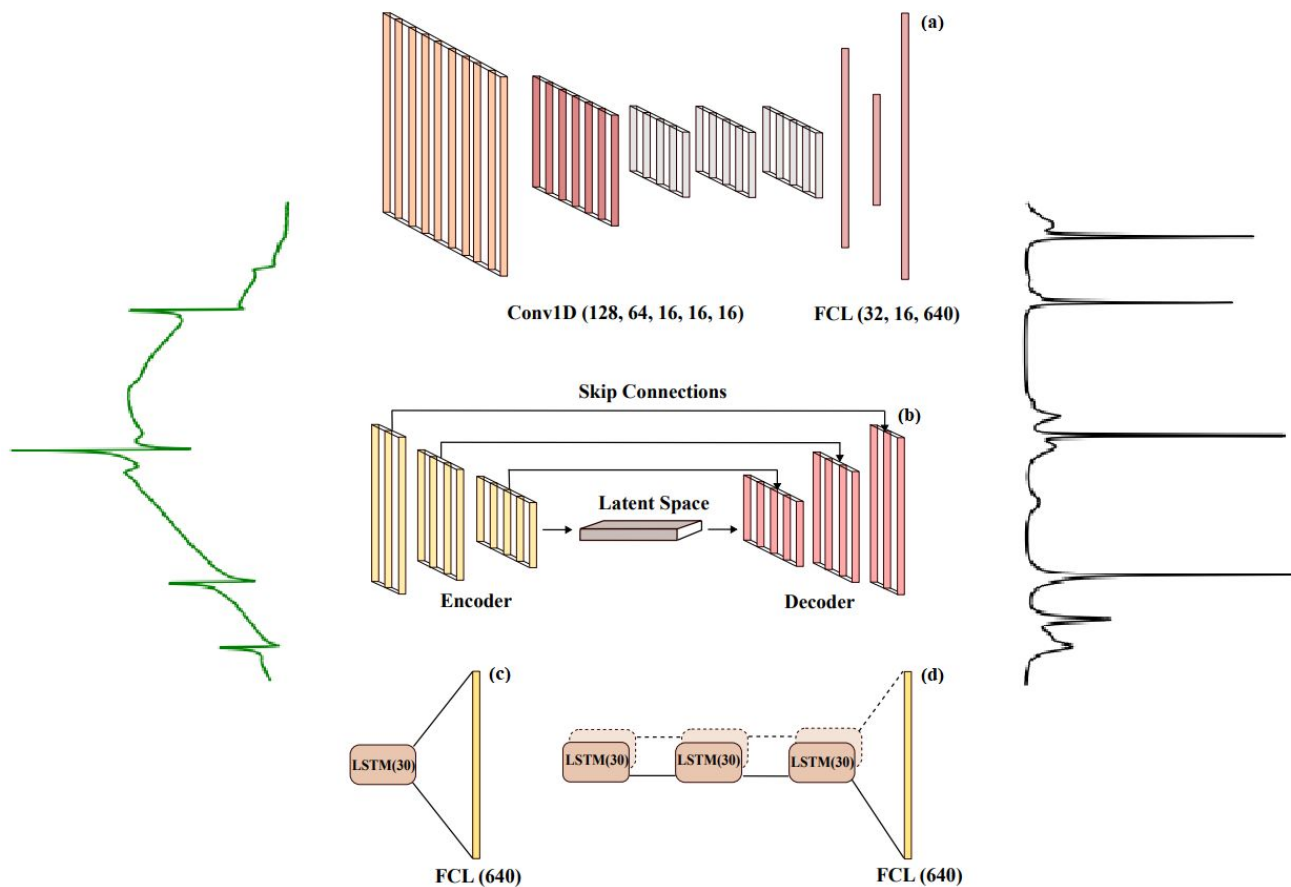


**Fig. 1** General schematic of the four models that are used including (a) convolutional neural network model, (b) autoencoder model, (cc) LSTM model and (d) Bi-LSTM model. The input for all four models is a CARS spectrum while the output is the corresponding Raman signal that is predicted by the models.

avoids the padding phenomenon that usually happens in convolutional layers. These skip connections speed up the training process and improve the model's performance in deeper networks compared to the plain ones. It also helps to mitigate the overfitting problem when the model is too complex and therefore improve the model generalization.

### 3.3 Long short-term memory (LSTM) neural network

A recurrent neural network (RNN) is a type of ANN that allows the modelling of temporal dynamic behaviour in the architecture by containing loops between the layers. This characteristic enables the data samples to be dependent on each other and memorization of previous information - a feature that traditional ANNs suffer from. However, RNNs suffer from a problem related to long-term dependencies, which means that if the delay/distance between the depending input samples or sequences increases, it cannot model such dependencies<sup>50</sup>. As a remedy for this problem, a long short-term memory (LSTM) network has been introduced<sup>51</sup>. The LSTM architecture is based upon four neural network layers, including the forget gate, input gate, output gate, and cell state.

The proposed LSTM architecture is adapted from this work<sup>30</sup>. Their code is not available for the direct reuse and its architecture is simple. It contains one LSTM layer of 30 units

with the ReLU as an activation function and Sigmoid as a recurrent activation function. The loss function is MSE, and the optimizer is Adam, while the learning rate is 0.005. They have simulated the CARS spectra with NRB as weak and strong regions.

### 3.4 Bi-Long short-term memory (Bi-LSTM) neural network

Bi-directional Long-Short Term Memory (Bi-LSTM)<sup>52</sup> network is a variant of the LSTM architecture that enables the input data sequence to be modelled in both directions, forward and backward. This is implemented by following the input sequence backward through an additional backward LSTM layer. Then the outputs of both forward and backward layers are combined through several ways including average, sum, multiplication, and concatenation. Using two LSTM layers improves the learning of the long-term dependencies and this leads to improved final accuracy of the model.

LSTM architecture is usually applied to ordered data without time labels like text classification or to constant time-sampling rate such as stock price predictions. All these are usually observed in irregular time-sampling rate. Hence a pre-processing method named functional principal component analysis (FPCA) was applied. Therefore, an additional dimension

is needed to contain the phase information of the spectrum. Hence the DL model should have an additional channel to contain it as the input data as well. LSTM does not have this channel so as the solution, the Bi-LSTM model has been used and the phase information was integrated as the input as well. The proposed Bi-LSTM architecture inspired from this work<sup>44</sup>. It consists of three bidirectional layers, each of them having 30 unit, and a time distributed fully connected layer as output, therefore, achieving an output for each time step. MSE and Nadam were used as the loss function and the optimizer respectively<sup>44</sup>.

## 4. Results and Discussion

In the following sections, the results of the four models are discussed. First, the models are evaluated on the simulated data and later experimentally measured CARS data.

### 4.1 Prediction on synthetic data

Initially, the efficiency of the four-trained models is demonstrated by retrieving the imaginary part from the 300 synthetic test spectra. These test spectra were independently generated apart from the training set where the spectral simulation parameter values are randomly selected from the given range of values as enumerated in table 1. The NRB utilized for generating training data is a 4<sup>th</sup> order polynomial function. However, three different NRBs were considered to simulate these 300 test spectra. Here, the idea is to estimate the four models' performance when they encounter the spectra simulated with NRB other than the 4<sup>th</sup> order polynomial function. Further, the first hundred spectra (1-100) of the 300 test spectra are simulated by considering the NRB as a 'Product of two Sigmoid', whereas spectra 101-200 are generated by assuming NRB as 'One sigmoid'. The last hundred (201-300) spectra were synthesized by adapting the NRB as a '4<sup>th</sup> order polynomial function'. These 300 synthetic test spectra are available here.<sup>43</sup>

#### 4.1.1 Extraction the imaginary part

Figure 2(a-d) represents the predicted imaginary part of the 295<sup>th</sup> test spectrum by the VECTOR, Bi-LSTM, CNN, and LSTM models, respectively. This spectrum is arbitrarily considered as an example from the entire test set only to visualize the efficacy of the four trained models. In each plot in the input CARS spectrum is presented at the top with green color. The true & predicted imaginary parts are shown in the middle, with black and green colors, respectively. The error between the true and predicted value is estimated then the square of the error (SE) is presented at the bottom with the blue line. This SE plot can be considered a visualization tool for validating the performance of the models. The four models extracted all the spectral lines, albeit their intensity has deviated from the actual one for some models, as shown in Figure 2(a-d). The estimated SE is found to be higher for LSTM, followed by the VECTOR, CNN, and Bi-LSTM, respectively.

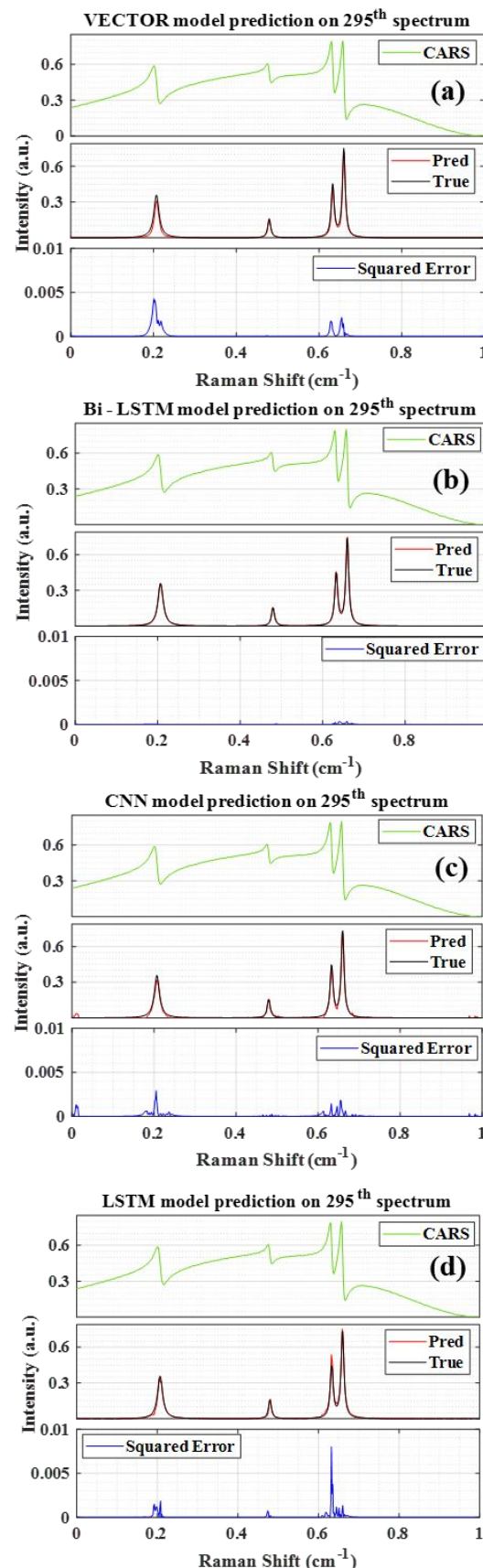


**Fig. 2** Comparison of the results obtained from the four models. a) VECTOR Prediction, b) Bi-LSTM Prediction, C) CNN Prediction, and d) LSTM Prediction. The labels 'True' & 'Pred' represent the true and predicted imaginary parts respectively.

## ARTICLE

## Journal Name

It is noticed that some peaks with lower intensity were observed on either side of the spectra for CNN, which were actually not present in the true Raman signal. These spurious lines can degrade the performance of the CNN compared to other models. In the case of LSTM, the predicted spectral line intensities are a little higher; on the contrary, it is slightly lower for the VECTOR prediction. Figure 2(c) illustrates the Raman signal retrieved from the Bi-LSTM model, where the extracted imaginary spectrum closely resembles the true spectrum. Also, it has not predicted any other spurious lines throughout the spectral range.

The SE plot visualization (represented at the bottom of the Figure, for example, see Figure 2a) efficaciously demonstrates the differences between the true and retrieved Raman signals throughout the spectral range for a single test spectrum. Nevertheless, visualization for the entire test set would not be feasible. Therefore, the mean square error (MSE) plot is considered for evaluating each trained model, as shown in Figure 3(a-d). The MSE is estimated by averaging the measured SE over 300 test spectra. The black dots in Figure 3(a-d) represent the average SE, and the red line corresponds to their standard deviation. For easy interpretation, the total spectral window can be divided into three parts first region ( $0\text{--}0.1\text{ cm}^{-1}$ ), mid-region ( $0.1\text{--}0.9\text{ cm}^{-1}$ ), and last region ( $0.6\text{--}1\text{ cm}^{-1}$ ), where the middle region itself accounts for 80 % of total data points, and the remaining 20 % represents first and last regions.

It is also observed that the error is less in the mid-region compared to the other two regions of the spectra. The measured MSE is highest in the first region compared to the remaining two regions, as shown in Figure 3(a-d). It is true for all four models, irrespective of their architecture. The standard deviation is found to be a maximum of  $\sim 0.06$  for the VECTOR and CNN, and it is slightly less for the LSTM  $\sim 0.055$ . However, a drastic change is observed in the case of the Bi-LSTM model, which has shown a 60 times lower standard deviation contrary to the other models, i.e., only  $\sim 0.0012$ . Also, the deviation is approximately the same throughout the spectral range except for a few points for the Bi-LSTM. However, the scenario is entirely different for the other three models. The deviation in the first region is more than 15 times compared to the mid-region for the VECTOR model, whereas it is 5 and 10 times for the LSTM and CNN models, respectively.

In the last region, the maximum deviation is observed for the CNN model, i.e.,  $\sim 0.035$ , whereas the minimum for the Bi-LSTM, i.e.,  $\sim 0.001$ . In the case of VECTOR, it is  $\sim 0.025$ , and it is  $\sim 0.005$  for the LSTM model. Also, the deviation is nearly the same in the mid and last regions for the LSTM. Overall, the MSE plot visually demonstrated that the Bi-LSTM model has a superior capability in predicting the imaginary part from the CARS spectra among all four models. The same behaviour is noticed for the mean absolute error (MAE) as shown in Figure 5 in supplementary data. In the following section, Pearson correlation analysis is performed. It provides a unique numerical parameter for each test spectrum, i.e., a correlation

coefficient. Hence, it can be utilized as a performance metric for validating the predictions of the four different models.

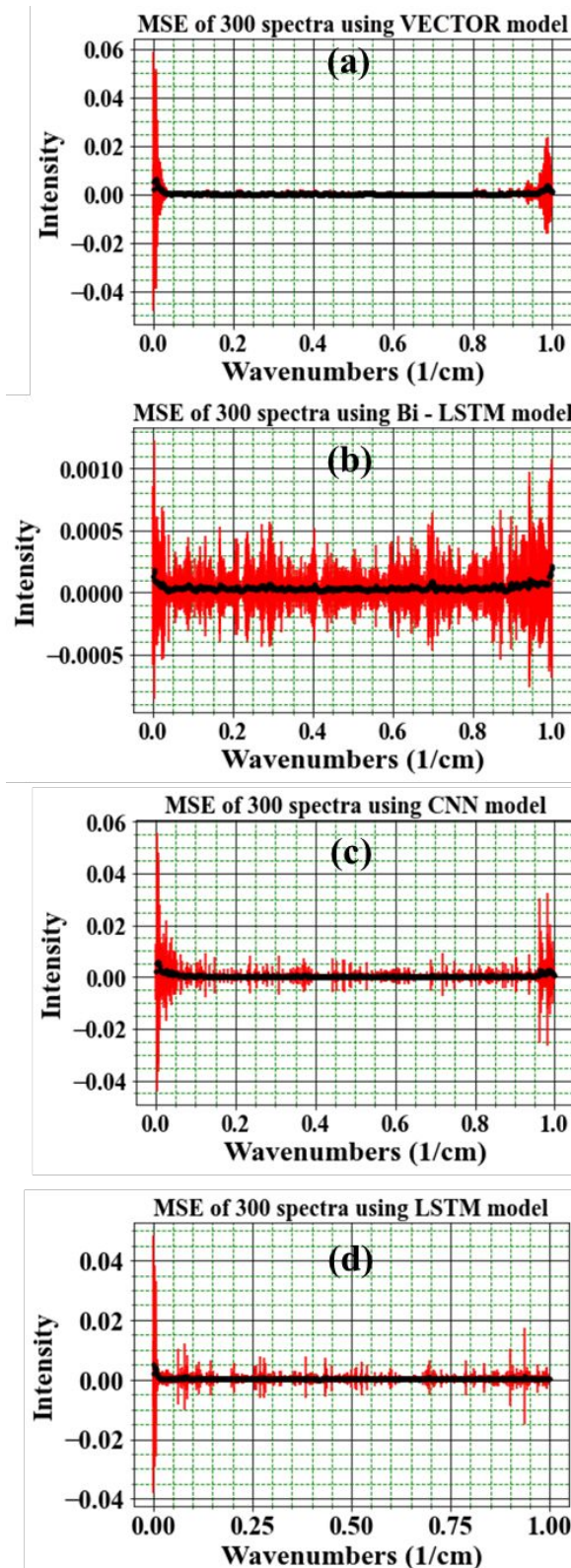


**Fig. 3 (a-d)** Represents the mean square error estimated for VECTOR, Bi-LSTM, CNN, and LSTM models, respectively. The black dots represent the mean value, whereas the red line corresponds to the standard deviation measured from the 300 test spectra.

#### 4.1.2 Pearson correlation analysis

It is a statistical approach that estimates the strength of the linear relationship between two sets of continuous variables and provides a unique numerical value, i.e., Pearson correlation coefficient (PCC)<sup>53</sup>. In this context, it represents a similarity percentage between the true and predicted imaginary parts of the CARS spectra. The measured PCC values can lie in the range of -1 and 1, which correspond to negative and positive linear correlation, respectively<sup>54</sup>. Overall, PCC value 1 represents the best match, i.e., true and predicted spectra are identical, whereas 0 corresponds to no similarity at all. Finally, the correlation analysis is performed on the imaginary parts predicted by the four models, and the results are presented in Figure 4(a-d), respectively. Two data points in the parathesis in Figure 4 represent the test spectrum number and its measured PCC value, respectively.

The PCC values estimated for the Bi-LSTM model have given higher coefficients compared to the other models for more than 97 % of test spectra, as shown in Figure 4(b).

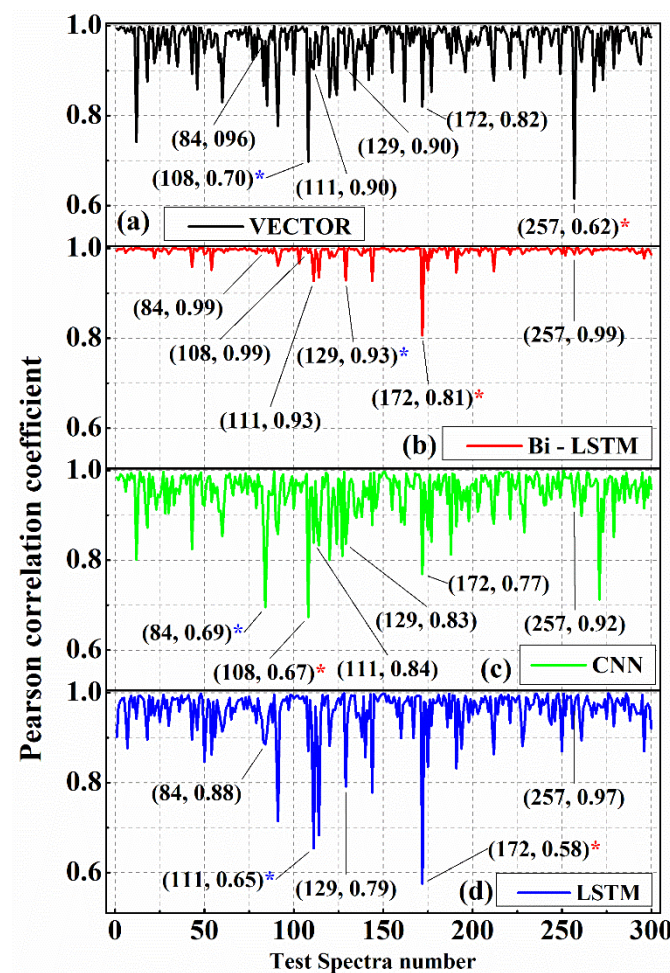


**Fig. 4** Pearson correlation coefficient (PCC) values estimated on predicted imaginary part by the a) VECTOR, b) LSTM, and c) CNN and d) LSTM models. The data points in the parenthesis represent the test spectrum number and its PCC value, respectively. A red asterisk denotes the lowest PCC value in the entire dataset. The blue asterisk represents the second-lowest PCC value.

Only one spectrum has given a PCC value of ~ 0.80 out of 300 spectra; all others have given PCCs of more than 0.92. In the case of CNN & VECTOR, four spectra have a PCC value less than 0.8, and it is five spectra for the LSTM model. Further, a histogram plot is drawn to graphically visualize the distribution of the estimated PCCs for the 300 test spectra, as shown in Figure 5. This plot presents the number of spectra that have the PCCs in a specific range, i.e., Frequency count in the selected PCC range. For example, seven spectra have PCC between 0.9-0.92 for the LSTM. Cumulatively, 273, 299, 264, and 273 spectra have PCCs > 0.9 for the VECTOR, Bi-LSTM, CNN, and LSTM models, respectively, which account for more than ~ 90 % of the test spectra. Hence, their distribution (on the x-axis) is presented only in the range of 0.9-1 instead of 0-1, which ascertains the best visualization of the PCCs distribution.

Also, it is noticed that 282 spectra have PCC values > 0.98 for the Bi-LSTM model, which corresponds to the ~94 % of total test data. It demonstrates that the Raman signal extracted using the Bi-LSTM model is in better agreement with the ground truth. On the other hand, only 102 and 131 spectra have PCC values > 0.98 for the CNN and LSTM models, respectively, which account for less than ~50 % of the total data. The CNN and LSTM models' performances were found to be almost the same when comparing their PCC values. Hence, the frequency count in most of the bins is approximately the same for the LSTM and CNN models. Further, their estimated PCCs difference is less than 0.05 for 253 spectra and less than 0.1 for 285 spectra, as shown in Figure 2 in supplementary data.

Further, it is observed that the maximum PCC value obtained is close to 1 for all the models. Nevertheless, the minimum values have shown a notable variation when compared with the predictions of the Bi-LSTM model. The lowest predicted PCC value is ~0.81 for the Bi-LSTM; meanwhile, it is ~0.58, ~0.62, and ~0.67 for the LSTM, VECTOR, and CNN models, respectively. The test spectrum with the lowest PCC value in each model is marked with a red asterisk (\*) for easy representation. For example, it is 257<sup>th</sup> spectrum for the VECTOR prediction, whereas it is 108<sup>th</sup> spectrum for CNN, and it is 172<sup>nd</sup> spectrum in the case of Bi-LSTM & LSTM models.

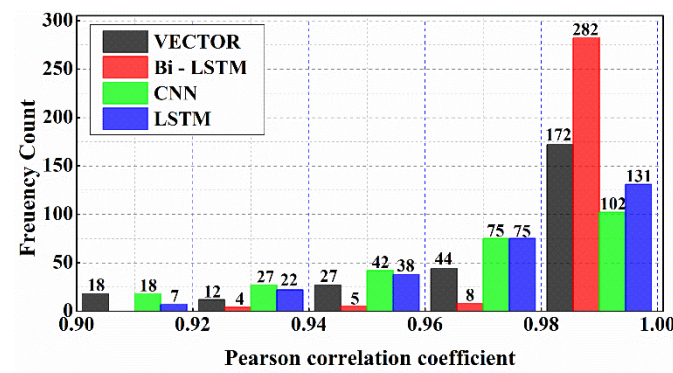


**Fig. 5** Histogram plot of the measured PCC values of the four models.

## ARTICLE

## Journal Name

The 2<sup>nd</sup> lowest PCC value is presented with a blue asterisk. These test spectra, along with their Raman line shapes extracted by the four models, are shown in Figure 6. These visualizations inherently represent the limitations of each model in retrieving the imaginary part from the CARS spectra. It also investigates the route cause for attaining the lowest PCC value for each trained model.

Figure 6(a1-a4) illustrates the results obtained from the 257<sup>th</sup> test spectrum using VECTOR, Bi-LSTM, CNN, and LSTM models, respectively. The input CARS spectrum has four spectral features in the entire spectral range where all the lines have higher intensity except for the peak at 0.66 cm<sup>-1</sup>. Among four lines, one is located near the right extrema, i.e., at 0.99 cm<sup>-1</sup>, and it could not be extracted by the VECTOR, whereas the other three models predicted it, but a huge error is found in the case of CNN. A similar observation was noticed in our previous work <sup>33</sup>, where the CNN prediction capability is poor at the edges. The LSTM and Bi-LSTM models have predicted all the lines, including the line at 0.99 cm<sup>-1</sup>, and the predictive performance was found to be the same for both models. Further, this inefficient extraction of the Raman line at 0.99 cm<sup>-1</sup> has given an SE of ~0.19 for the VECTOR and led to the minimum PCC value in the entire test dataset, i.e., ~0.62. The SE for the Bi-LSTM, LSTM, and CNN is ~0.005, ~0.01, and ~0.08, respectively.

Figure 6(b1-b4) shows the results of the 172<sup>nd</sup> test spectrum obtained from the VECTOR, Bi-LSTM, CNN, and LSTM models, respectively. The input CARS spectrum has one strong line at ~0.86 cm<sup>-1</sup> and three very faint spectral lines in the remaining spectral range. These faint lines' intensities are close to the noise level. Also, the maximum spectral line intensity is only ~0.062, and due to this, the spectrum looks noisy compared to other test spectra where the intensities are higher by more than order. All four models predicted only one line at ~0.86 cm<sup>-1</sup>, and the rest of the lines were not extracted properly. Further, the predicted intensities are matched with the true one for the Bi-LSTM where the lowest SE is noticed, i.e., ~0.001, and the SE is 4, 48, and 18 times more for the VECTOR, LSTM, and CNN models, respectively. It is also observed that all the models have predicted some spurious lines with minute intensities throughout the spectral range. These observations affected the PCC measurements, and hence lowest coefficients, ~0.81 and ~0.58 are achieved for Bi-LSTM and LSTM models, respectively.

Figure 6(c1-c4) illustrates the 108<sup>th</sup> test spectrum results obtained from the VECTOR, Bi-LSTM, CNN, and LSTM models, respectively. The input CASRS spectrum has several vibrational spectral features with different peak intensities. Nevertheless, the first spectral line at ~0.006 cm<sup>-1</sup> (on the left extreme) has only half part, i.e., the spectral line is started with the trailing part instead of the rising part. It is observed due to considering the spectral line/peak generation anywhere on the entire spectral range (0-1) during the CARS spectra simulation. So, the lines generated close to the extremes sometimes have either a rising or trailing part depending on the peak position and width.

Hence, the error may also occur on the right side of the spectrum, as reported in our previous study <sup>33</sup>. The CNN and VECTOR models have predicted all the Raman lines except for the first line at ~0.006 cm<sup>-1</sup>, which is due to considering only half part of the spectral line. Similar observations were also noticed in the previous studies where the CNN model performance deteriorated when it encountered the spectral lines, with only having either a rising or trailing part <sup>33</sup>. This inherent constraint has given a high SE of ~0.15 and affected the PCC measurements, where its value is minimum (~0.67) for the CNN model and the second lowest PCC value (~0.70) for the VECTOR model. This could be a reason for the high MSE observed on either side of the extrema for the VECTOR and CNN models, as shown in Figure 3(a & c), respectively. Further, the Bi-LSTM and LSTM have predicted all the lines, including the first one on the left end. However, the LSTM model has given a high error compared to the Bi-LSTM model, which is of more than order.

Further, the test spectra corresponding to the second lowest PCC value are presented in supplementary Figure 3. It is the 84<sup>th</sup> spectrum for the CNN (~0.69) and 111<sup>th</sup> spectrum for the LSTM (~0.65), and 129<sup>th</sup> spectrum for the Bi-LSTM (~0.93) model. The results of the 111<sup>th</sup> spectrum are presented in supplementary Figure 3 (a1-a4), where the two spectral features are not predicted by the four models. These two spectral lines are very faint. Also, the predicted intestines have deviated, and the error is highest for the LSTM, which is reflected in PCC measurements, and the error is minimum for the Bi-LSTM. The results of the 129<sup>th</sup> test spectrum are shown in supplementary Figure 3(b1-b4), where the input CARS spectral lines intensity is low. The SE of the spectral line at ~0.97 (on the right extreme) is only ~0.004 for the Bi-LSTM, whereas it is more than 20 times for the other three models. However, the Bi-LSTM could not able to predict the two lines, which led to 2<sup>nd</sup> lowest PCC value. Further, the other three models also not retrieved three/four lines. In the case of the 84<sup>th</sup> spectrum, four models have predicted all the lines. Nevertheless, the retrieved peak intensities are deviated for all the models except for Bi-LSTM, as shown in supplementary Figure 3 (c1-c4). The deviation is found to be maximum for the CNN, followed by the LSTM, VECTOR, and Bi-LSTM, respectively. The SE of the spectral line at ~0.97 (on the right extreme) is only ~0.002 for the Bi-LSTM, whereas it is 30, 22, and 13 times more for the CNN, LSTM, and VECTOR models, respectively. These visual findings clearly demonstrate that the Bi-LSTM model has superior capability in predicting imaginary parts compared to the other three models.

In conclusion, Figures (4 & 6) and supplementary Figure 3 have visually demonstrated the imaginary part prediction capability of four models where the performance of the Bi-LSTM model was found to be best. Numerically, it performed well on more than 97 % of the total test dataset (i.e., it has a higher PCC value than the other three models). It also revealed that the Bi-LSTM model has better capability when extracting spectral lines at the ends, even though they only have either a rising or trailing part which led to the lowest MSE even at the edges, as shown in Figure 3(b).

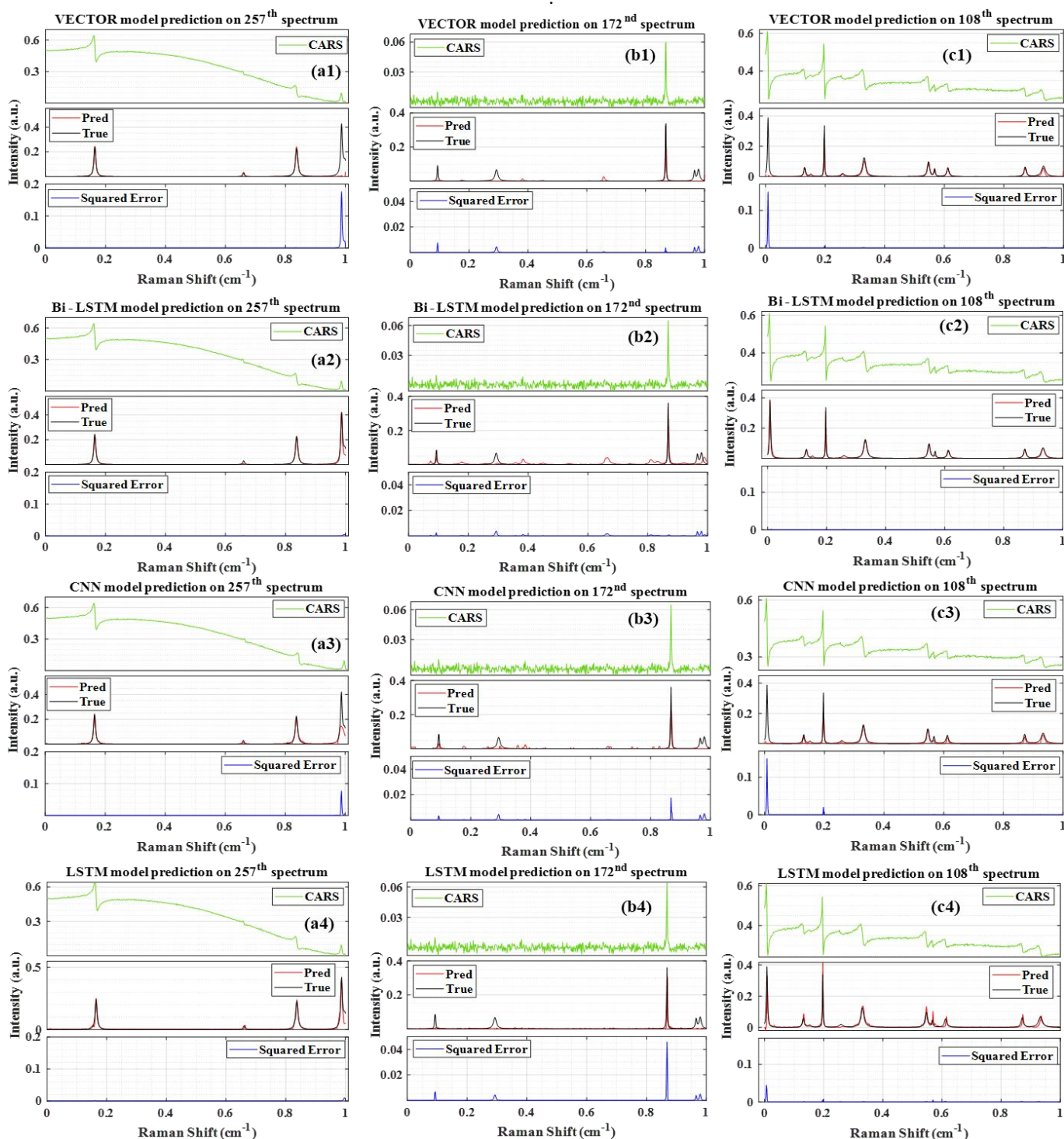


Fig. 6 Comparison of the results obtained from the four models. (a1-a2) Raman signal extracted from the 257<sup>th</sup> test spectra using VECTOR, Bi-LSTM, CNN, and LSTM models, respectively. (b1-b4) results of 172<sup>nd</sup> spectrum, (c1-c4) results of the 108<sup>th</sup> spectrum. 'Pred' is the predicted Raman signal, and 'True' represents the actual Raman signal. Squared error corresponds to their difference.

Further, the efficiency decreased when only it encountered the noisy CARS spectrum with very low intensity. The results of the experimental CARS spectra are discussed in detail in the next section.

#### 4.2 Prediction on experimental CARS spectra

This section critically examines the four trained model's potential by retrieving the Raman signal from the experimentally recorded CARS spectra. This detailed interrogation provides a comprehensive overview of the

## ARTICLE

## Journal Name

model's performance when working with the real CARS data, viz., ADP/AMP/ATP mixture, DMPC, yeast, and protein samples. These biological samples have different resonance vibrational bands with various backgrounds. The sample preparation details and experimental setup overview is presented in section 2.2.

Figure 7 visualizes the results obtained from the four models on these experimental CARS data. Each plot in Figure 7 is a three-stacked plot (see Figure 7(a) for reference). The first row represents the input CARS spectrum (green line), and the second row visualizes the true (black line) and predicted (red line) imaginary parts. The labels 'True' and 'Pred' in the Figure correspond to the imaginary part extracted by the Maximum Entropy method and trained DL models, respectively. Further, the third row represents the square of the error (blue line), i.e., the square of the difference between the predicted and true imaginary parts. In each sample, the y-axis scale is considered to be the same for all four models for better visualization.

Figure 7(a1-a4) represents the results of the protein sample in the fingerprint region ( $700\text{--}1900\text{ cm}^{-1}$ ) obtained from the VECTOR, Bi-LSTM, CNN, and LSTM models, respectively. It has various resonance vibrational bands, including tyrosine peaks at 850, 1210, and  $1616\text{ cm}^{-1}$ , Amide I bands ( $\sim 1220\text{--}1250\text{ cm}^{-1}$ ), Amide III bands ( $\sim 1600\text{--}1700\text{ cm}^{-1}$ ), and CH<sub>2</sub> band at  $1445\text{ cm}^{-1}$ . Here the prediction of the Bi-LSTM model is in good agreement with the true one, where the SE is only  $\sim 0.02$ . In contrast, the LSTM model prediction is poor, where the extracted line shapes are very broad, and intensities deviate from the true ones. The other two models also predicted the spectral lines, albeit the intensities differed from the actual signal. Hence, the SE is found to be 6 times more for the VECTOR model compared to the Bi-LSTM, and it is 20 times for the LSTM and 5 times for the CNN. These observations are reflected in PCC measurements as shown in Figure 9(a), where the highest value is obtained for the Bi-LSTM, i.e.,  $\sim 0.95$ , and the minimum for the LSTM  $\sim 0.42$ . The other two have given the same value,  $\sim 0.89$ .

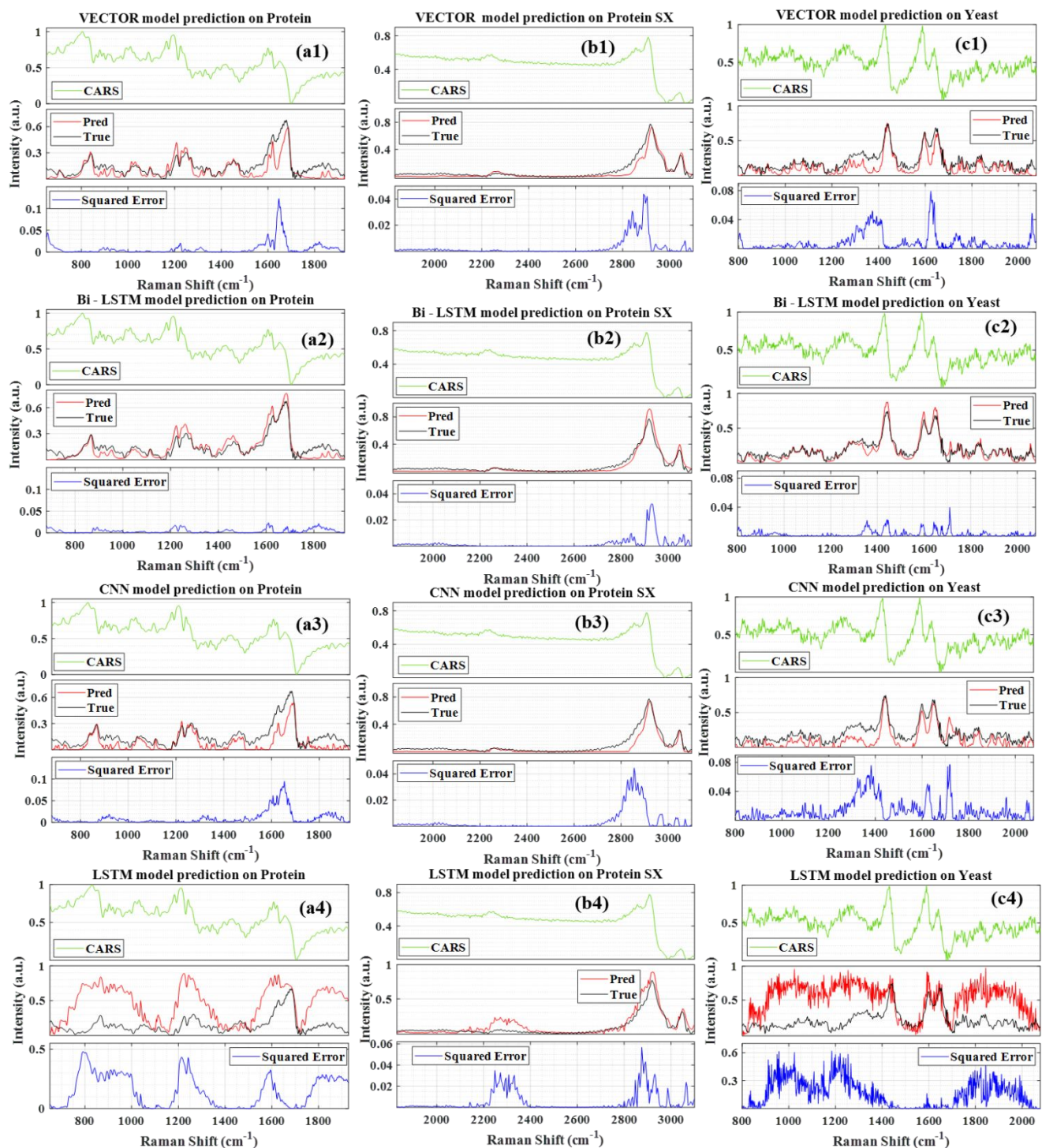
Figures 7(b1-b4) represent the results of the protein sample in the range of  $1830\text{--}3100\text{ cm}^{-1}$  from the VECTOR, Bi-LSTM, CNN, and LSTM models, respectively. The predicted line shapes are matching with true one for the Bi-LSTM, but the peak intensities have slightly deviated. On the contrary, the CNN and VECTOR models have correctly extracted the peak intensities; however, the line shapes have deteriorated. Similar behaviour is noticed for the LSTM, and in addition, a broad spurious peak is also observed in the spectral range of  $2200\text{--}2400\text{ cm}^{-1}$ . Overall minimum SE  $\sim 0.032$  is noticed for the Bi-LSTM and a maximum for the LSTM  $\sim 0.059$ .

Figure 7(c1-c4) illustrates the imaginary part retrieved from the yeast sample by these four models, respectively. All the models except for the LSTM have extracted major resonance spectral features (C-H bend of the aliphatic chain at  $1440\text{ cm}^{-1}$ , amide band at  $1654\text{ cm}^{-1}$ , C=C bending mode of phenylalanine at

$\sim 1590\text{ cm}^{-1}$ ); nonetheless, the predicted intensities have deviated for the VECTOR and CNN models compared to the Bi-LSTM. In the case of LSTM, an intense ringing structure has appeared throughout the spectral region, excluding resonance peak positions that are not present in the true Raman spectra. The maximum estimated SE for Bi-LSTM is  $\sim 0.04$ , and it is more than two times for the LSTM and CNN. The error is more than an order for the LSTM due to the deteriorated spectral line shapes. The measured PCC values also conveyed the same information where predictive performance is superior for the Bi-LSTM ( $\sim 0.96$ ) model followed by the VECTOR ( $\sim 0.92$ ), CNN ( $\sim 0.89$ ), and LSTM ( $\sim 0.41$ ) as shown in Figure 9(a).

The results of the ADP/AMP/ATP mixture obtained by the VECTOR, Bi-LSTM, and LSTM are presented in Figure 8 (a1-a3). The CNN model prediction can be found here<sup>35</sup>. The adenine vibrations are observed in the range of  $1270\text{--}1400\text{ cm}^{-1}$ , and the strongest one is noticed at  $\sim 1330\text{ cm}^{-1}$  as shown in Figure 8 (a1-a3)<sup>55</sup>. All four models have retrieved these adenine vibrations, albeit the extracted line intensities are not matching with the true intensities. The measured SE in this spectral range is noticed maximum for the VECTOR models ( $\sim 0.003$ ), followed by the LSMT ( $\sim 0.04$ ), Bi-LSTM ( $\sim 0.004$ ), and CNN ( $\sim 0.001$ )<sup>56</sup>. Further, the symmetric stretching vibration of the triphosphate group of ATP ( $\sim 1123\text{ cm}^{-1}$ ) is retrieved by all the models except for the LSTM. Hence the highest SE is observed for the LSTM ( $\sim 0.36$ ) and the minimum for the CNN ( $\sim 10^{-5}$ ). In the case of Bi-LSTM, the SE is  $\sim 10^{-4}$ , and it is  $\sim 10^{-2}$  for the VECTOR. Similar behaviour is noticed for the diphosphate resonance band ( $\sim 1100\text{ cm}^{-1}$ ). The monophosphate resonance band of AMP ( $979\text{ cm}^{-1}$ ) is only extracted by Bi-LSTM and CNN. The LSTM and VECTOR models could not able to predict it and led high SE. Here also, PCC values measured for all four models where the Bi-LSTM and CNN are the best among all as they have the highest coefficient  $\sim 0.93$ , followed by VECTOR ( $\sim 0.85$ ) and LSTM ( $\sim 0.42$ ).

Figure 8 (b1-b3) depicts the results of the DMPC sample retrieved from the VECTOR, Bi-LSTM, and LSTM models, respectively. The results of the CNN can be found here<sup>35</sup>. Prominent vibrational bands such as CH Strech mode, symmetric and antisymmetric stretching modes of methylene groups, and overtone of the methylene scissoring mode appeared in the range of  $2600\text{--}3000\text{ cm}^{-1}$ <sup>57,58</sup>. All four models have extracted these vibrational bands except for the LSTM. It could not able to predict the vibrational mode at  $2946\text{ cm}^{-1}$  and led to a high error. Also, a strong spurious line appeared on the right extreme for the LSTM prediction. These observations have affected the PCC measurements, where the PCCs values are  $\sim 0.8$ ,  $\sim 0.93$ ,  $\sim 0.89$ , and  $\sim 0.42$  for the VECTOR, Bi-LSTM, CNN, and LSTM models, respectively as shown in Figure 9(a). The Bi-LSTM model performance was found to be the best among all, where the highest average correlation coefficient is obtained for the Bi-LSTM, followed by CNN, VECTOR, and LSTM models, respectively, as shown in Figure 9(b). However, a relatively higher computational time is required for Bi-LSTM, as presented in Table 1 in supplementary data.



**Fig. 7** Results of the experimental CARS spectra. (a1-a4) the imaginary parts predicted by the VECTOR, Bi-LSTM, CNN, and LSTM models for the protein sample in the spectral range of 800–1800 cm<sup>-1</sup>, respectively. (b1-b4) prediction of the protein sample in the spectral range of 1830–3100 cm<sup>-1</sup>. (c1-c4) predictions on Yeast sample.

Overall, the BLSTM model predictions are optimum not only on the synthetic data but also on the experimental data. However, a few limitations were noticed when evaluating it on the spectra with low spectral line intensities and higher noise levels where it could not able to find some peaks. These observations suggest that modification of the spectral simulation parameters is required. Especially we are planning to train the model with

data generated by different noise levels in our future work. It would also be interesting to train the model with data generated by different simulation parameters (number of peaks, frequencies, amplitudes, etc.) to fit specific applications in different spectral regions<sup>59</sup>. Also, fine-tuning or transferring learning mechanisms can be explored to circumvent these limitations, which positively impacts model performance.

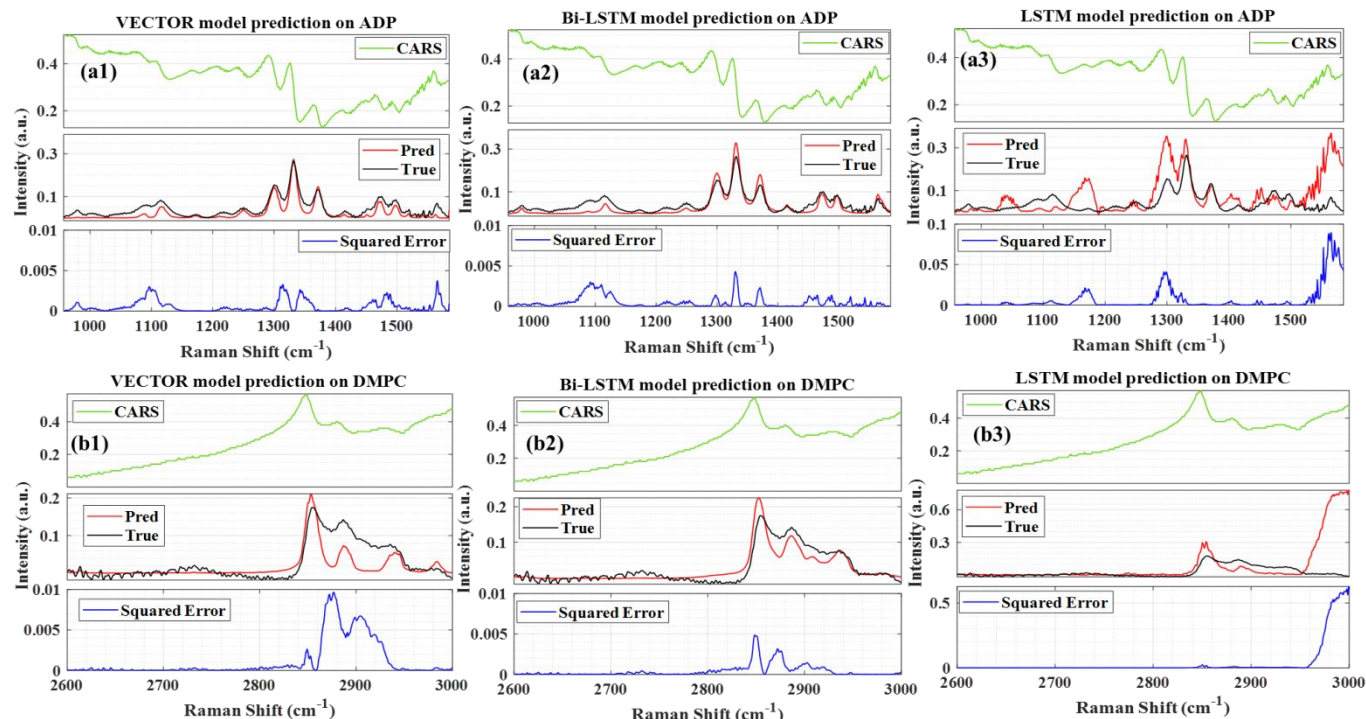


**Fig. 8** Results of the experimental CARS spectra. (a1-a3) the imaginary parts predicted by the VECTOR, Bi-LSTM and LSTM models for the ADP/AMP/ATP mixture, respectively. (b1-b3) predictions on DMPC sample.

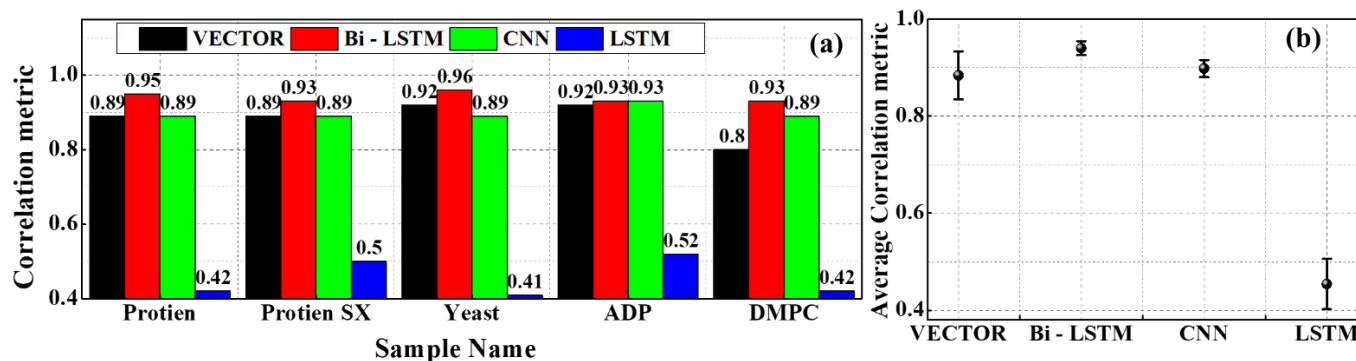


**Fig. 9** a) The PCCs values measured on the experimental CARS predictions using four trained models. b) The average value of the PCCs estimated from the five experimental CARS data.

## 5. Conclusions

We have systematically evaluated four DL models, namely CNN, LSTM, VECTOR, and Bi – LSTM, to retrieve the Raman signals from the CARS spectra. These four algorithms fundamentally differ from each other and provide a comprehensive overview in the context of applying them to CARS data analysis. All the models were trained with CARS simulated with the NRBs as a fourth-order polynomial function. The test dataset (300 spectra) is independently generated where three different NRBs (fourth-order polynomial function, product of two Sigmoid, and Single Sigmoid) are considered for every 100 spectra. The predictions of the test spectra revealed that Bi-

LSTM performance is superior, where the measured mean square error is 60 times less compared to the other three models. Also, it predicted the spectral lines on either end of the spectra, but the other three models could not able to extract the same. Further, the correlation analysis revealed that 97 % of test data has a higher correlation coefficient for the Bi-LSTM model than the other three models. Also, ~94 % of total test spectra have PCC values > 0.98 for the Bi-LSTM model, whereas 57 % for the VECTOR, 34 % for the LSTM, and 44 % for the CNN model. Finally, the predictions on four experimental samples (Protein, DMPC, ADP, and Yeast) also confirmed the same, where the predictive capability is best for the Bi-LSTM model compared to the other three. This systematic study shows that the Bi-LSTM model has great potential and provides a giant leap toward analysing the CARS data.

## Author Contributions

Rajendhar Junjuri (RJ), Lasse Lensu (LL), Erik M. Vartiainen (EMV) have conceived the idea of the experiment. Rajendhar Junjuri (RJ) has performed the analysis and prepared the initial Draft. Ali Saghi (AS), has trained VECTOR model and also contributed to the analysis part. Finally, the draft was revised by LL, EMV, and AS.

## Conflicts of interest

There are no conflicts to declare.

## Acknowledgements

This work is a part of the “Quantitative Chemically-Specific Imaging Infrastructure for Material and Life Sciences (qCSI)” project funded by the Academy of Finland (Grant No. FIRI/327734). Also, we thank Michiel Müller and Hilde Rinia for providing the experimental measurements of the DMPC lipid sample and the AMP/ADP/ATP mixture, as well as, Masanari Okuno and Hideaki Kano for providing the experimental measurements of the yeast sample and Yelena Kan and Sapun Parekh for providing the protein droplet measurements.

## References

- 1 A. Zumbusch, G. R. Holtom and X. S. Xie, Three-dimensional vibrational imaging by coherent anti-Stokes Raman scattering, *Phys. Rev. Lett.*, 1999, **82**, 4142.
- 2 L. M. Malard, L. Lafeta, R. S. Cunha, R. Nadas, A. Gadelha, L. G. Cançado and A. Jorio, Studying 2D materials with advanced Raman spectroscopy: CARS, SRS and TERS, *Phys. Chem. Chem. Phys.*, 2021, **23**, 23428–23444.
- 3 K. I. Popov, A. F. Pegoraro, A. Stolow and L. Ramunno, Image formation in CARS and SRS: effect of an inhomogeneous nonresonant background medium, *Opt. Lett.*, 2012, **37**, 473–475.
- 4 G. I. Petrov, R. Arora and V. V. Yakovlev, Coherent anti-Stokes Raman scattering imaging of microcalcifications associated with breast cancer, *Analyst*, 2021, **146**, 1253–1259.
- 5 C. L. Evans and X. S. Xie, Coherent anti-Stokes Raman scattering microscopy: chemical imaging for biology and medicine, *Annu. Rev. Anal. Chem.*, 2008, **1**, 883–909.
- 6 O. Burkacky, A. Zumbusch, C. Brackmann and A. Enejder, Dual-pump coherent anti-Stokes-Raman scattering microscopy, *Opt. Lett.*, 2006, **31**, 3656–3658.
- 7 F. Ganikhanov, C. L. Evans, B. G. Saar and X. S. Xie, High-sensitivity vibrational imaging with frequency modulation coherent anti-Stokes Raman scattering (FM CARS) microscopy, *Opt. Lett.*, 2006, **31**, 1872–1874.
- 8 J.-X. Cheng, L. D. Book and X. S. Xie, Polarization coherent anti-Stokes Raman scattering microscopy, *Opt. Lett.*, 2001, **26**, 1341–1343.
- 9 M. Jurna, J. P. Korterik, C. Otto, J. L. Herek and H. L. Offerhaus, Background free CARS imaging by phase sensitive heterodyne CARS, *Opt. Express*, 2008, **16**, 15863–15869.
- 10 S. O. Konorov, M. W. Blades and R. F. B. Turner, Lorentzian amplitude and phase pulse shaping for nonresonant background suppression and enhanced spectral resolution in coherent anti-Stokes Raman scattering spectroscopy and microscopy, *Appl. Spectrosc.*, 2010, **64**, 767–774.
- 11 M. Müller and A. Zumbusch, Coherent anti-Stokes Raman scattering microscopy, *ChemPhysChem*, 2007, **8**, 2156–2170.
- 12 M. Cui, B. R. Bachler and J. P. Ogilvie, Comparing coherent and spontaneous Raman scattering under biological imaging conditions, *Opt. Lett.*, 2009, **34**, 773–775.
- 13 E. M. Vartiainen, Phase retrieval approach for coherent anti-Stokes Raman scattering spectrum analysis, *JOSA B*, 1992, **9**, 1209–1214.
- 14 Y. Liu, Y. J. Lee and M. T. Cicerone, Broadband CARS spectral phase retrieval using a time-domain Kramers–Kronig transform, *Opt. Lett.*, 2009, **34**, 1363–1365.
- 15 C. H. Camp Jr, Y. J. Lee and M. T. Cicerone, Quantitative, comparable coherent anti-Stokes Raman scattering (CARS) spectroscopy: correcting errors in phase retrieval, *J. Raman Spectrosc.*, 2016, **47**, 408–415.
- 16 C. H. Camp Jr, J. S. Bender and Y. J. Lee, Real-time and high-throughput Raman signal extraction and processing in CARS hyperspectral imaging, *Opt. Express*, 2020, **28**, 20422–20437.
- 17 Y. Kan, L. Lensu, G. Hehl, A. Volkmer and E. M. Vartiainen, Wavelet prism decomposition analysis applied to CARS spectroscopy: a tool for accurate and quantitative extraction of resonant vibrational responses, *Opt. Express*, 2016, **24**, 11905–11916.
- 18 C. H. Camp, Raman signal extraction from CARS spectra using a learned-matrix representation of the discrete Hilbert transform, *Opt. Express*, 2022, **30**, 26057–26071.
- 19 Y. LeCun, Y. Bengio and G. Hinton, Deep learning, *Nature*, 2015, **521**, 436–444.
- 20 J. N. K. Liu, Y. Hu, Y. He, P. W. Chan and L. Lai, in *Information Granularity, Big Data, and Computational Intelligence*, Springer, 2015, pp. 389–408.
- 21 L. Deng and Y. Liu, *Deep learning in natural language processing*, Springer, 2018.
- 22 Y. Guo, Y. Liu, A. Oerlemans, S. Lao, S. Wu and M. S. Lew, Deep learning for visual understanding: A review, *Neurocomputing*, 2016, **187**, 27–48.
- 23 F. Lussier, V. Thibault, B. Charron, G. Q. Wallace and J.-F. Masson, Deep learning and artificial intelligence methods for Raman and surface-enhanced Raman scattering, *TrAC Trends Anal. Chem.*, 2020, **124**, 115796.
- 24 J. Yang, J. Xu, X. Zhang, C. Wu, T. Lin and Y. Ying, Deep learning for vibrational spectral analysis: Recent progress and a practical guide, *Anal. Chim. Acta*, 2019, **1081**, 6–17.
- 25 R. Luo, J. Popp and T. Bocklitz, Deep Learning for Raman Spectroscopy: A Review, *Analytica*, 2022, **3**, 287–301.
- 26 K. Ghosh, A. Stuke, M. Todorović, P. B. Jørgensen, M. N. Schmidt, A. Vehtari and P. Rinke, Deep learning

## ARTICLE

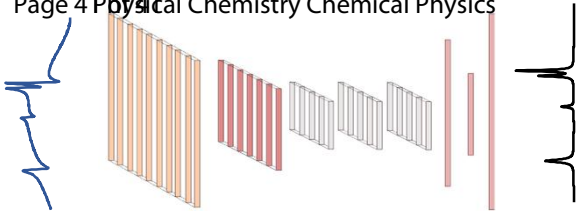
## Journal Name

- spectroscopy: Neural networks for molecular excitation spectra, *Adv. Sci.*, 2019, **6**, 1801367.
- 27 S. K. Anubham, R. Junjuri, A. K. Myakalwar and M. K. Gundawar, An approach to reduce the sample consumption for LIBS based identification of explosive materials, *Def. Sci. J.*, DOI:10.14429/dsj.67.10690.
- 28 E. Mal, R. Junjuri, M. K. Gundawar and A. Khare, Temporal characterization of laser-induced plasma of tungsten in air, *Laser Part. Beams*, 2020, **38**, 14–24.
- 29 R. Junjuri, S. A. Nalam, E. Manikanta, S. S. Harsha, P. P. Kiran and M. K. Gundawar, Spatio-temporal characterization of ablative Cu plasma produced by femtosecond filaments, *Opt. Express*, 2021, **29**, 10395.
- 30 R. Houhou, P. Barman, M. Schmitt, T. Meyer, J. Popp and T. Bocklitz, Deep learning as phase retrieval tool for CARS spectra, *Opt. Express*, 2020, **28**, 21002–21024.
- 31 C. M. Valensise, A. Giuseppi, F. Vernuccio, A. De la Cadena, G. Cerullo and D. Polli, Removing non-resonant background from CARS spectra via deep learning, *APL Photonics*, 2020, **5**, 61305.
- 32 Z. Wang, K. O' Dwyer, R. Muddiman, T. Ward, C. H. Camp and B. M. Hennelly, VECTOR: Very deep convolutional autoencoders for non-resonant background removal in broadband coherent anti-Stokes Raman scattering, *J. Raman Spectrosc.*, 2022, **53**, 1081–1093.
- 33 R. Junjuri, A. Saghi, L. Lensu and E. M. Vartiainen, Convolutional neural network-based retrieval of Raman signals from CARS spectra, *Opt. Contin.*, 2022, **1**, 1324.
- 34 A. Saghi, R. Junjuri, L. Lensu and E. Vartiainen, Semi-synthetic data generation to fine-tune a convolutional neural network for retrieving Raman signals from CARS spectra, *Opt. Contin.*, DOI:10.1364/OPTCON.469753.
- 35 R. Junjuri, A. Saghi, L. Lensu and E. M. Vartiainen, Effect of non-resonant background on the extraction of Raman signals from CARS spectra using deep neural networks, *RSC Adv.*, 2022, **12**, 28755–28766.
- 36 R. Junjuri, Four DL models evaluation on CARS data, <https://github.com/Junjuri/Four-DL-models-comparison-for-evaluating-CARS>.
- 37 M. Müller and J. M. Schins, Imaging the thermodynamic state of lipid membranes with multiplex CARS microscopy, *J. Phys. Chem. B*, 2002, **106**, 3715–3723.
- 38 M. Okuno, H. Kano, P. Leproux, V. Couderc, J. P. R. Day, M. Bonn and H. Hamaguchi, Quantitative CARS molecular fingerprinting of single living cells with the use of the maximum entropy method, *Angew. Chem. Int. Ed. Engl.*, 2010, **122**, 6925–6929.
- 39 A. C. Murthy, G. L. Dignon, Y. Kan, G. H. Zerze, S. H. Parekh, J. Mittal and N. L. Fawzi, Molecular interactions underlying liquid– liquid phase separation of the FUS low-complexity domain, *Nat. Struct. Mol. Biol.*, 2019, **26**, 637–648.
- 40 S. Chatterjee, Y. Kan, M. Brzezinski, K. Koynov, R. M. Regy, A. C. Murthy, K. A. Burke, J. J. Michels, J. Mittal and N. L. Fawzi, Reversible kinetic trapping of fus biomolecular condensates, *Adv. Sci.*, 2022, **9**, 2104247.
- 41 E. M. Vartiainen, H. A. Rinia, M. Müller and M. Bonn, Direct extraction of Raman line-shapes from congested CARS spectra, *Opt. Express*, 2006, **14**, 3622–3630.
- 42 VECTOR-CARS, <https://github.com/villawang/VECTOR-CARS>.
- 43 R. Junjuri, CARS data analysis with different NRB, <https://github.com/Junjuri/LUT>.
- 44 L. Hu, X. Chen and L. Wang, Spectroscopic Studies of Type Ia Supernovae Using LSTM Neural Networks, *Astrophys. J.*, 2022, **930**, 70.
- 45 G. E. Hinton, A. Krizhevsky and S. D. Wang, in *International conference on artificial neural networks*, Springer, 2011, pp. 44–51.
- 46 A. Géron, *Hands-on machine learning with Scikit-Learn, Keras, and TensorFlow*, 'O'Reilly Media, Inc.', 2022.
- 47 C.-Y. Liou, J.-C. Huang and W.-C. Yang, Modeling word perception using the Elman network, *Neurocomputing*, 2008, **71**, 3150–3157.
- 48 J. Schmidhuber, Deep learning in neural networks: An overview, *Neural networks*, 2015, **61**, 85–117.
- 49 K. He, X. Zhang, S. Ren and J. Sun, in *Proceedings of the IEEE conference on computer vision and pattern recognition*, 2016, pp. 770–778.
- 50 Z. C. Lipton, J. Berkowitz and C. Elkan, A critical review of recurrent neural networks for sequence learning, *arXiv Prepr. arXiv1506.00019*.
- 51 S. Hochreiter and J. Schmidhuber, Long short-term memory, *Neural Comput.*, 1997, **9**, 1735–1780.
- 52 M. Schuster and K. K. Paliwal, Bidirectional recurrent neural networks, *IEEE Trans. Signal Process.*, 1997, **45**, 2673–2681.
- 53 X. Tan, X. Chen and S. Song, A computational study of spectral matching algorithms for identifying Raman spectra of polycyclic aromatic hydrocarbons, *J. Raman Spectrosc.*, 2017, **48**, 113–118.
- 54 P. Schober, C. Boer and L. A. Schwarte, Correlation coefficients: appropriate use and interpretation, *Anesth. Analg.*, 2018, **126**, 1763–1768.
- 55 K. T. Yue, C. L. Martin, D. Chen, P. Nelson, D. L. Sloan and R. Callender, Raman spectroscopy of oxidized and reduced nicotinamide adenine dinucleotides, *Biochemistry*, 1986, **25**, 4941–4947.
- 56 L. Rimai, T. Cole, J. L. Parsons, J. T. Hickmott Jr and E. B. Carew, Studies of Raman spectra of water solutions of adenosine tri-, di-, and monophosphate and some related compounds, *Biophys. J.*, 1969, **9**, 320–329.
- 57 R. Mendelsohn and D. J. Moore, Vibrational spectroscopic studies of lipid domains in biomembranes and model systems, *Chem. Phys. Lipids*, 1998, **96**, 141–157.
- 58 A. Fasanella, K. Cosentino, A. Beneduci, G. Chidichimo, E. Cazzanelli, R. C. Barberi and M. Castriota, Thermal structural evolutions of DMPC-water biomimetic systems investigated by Raman Spectroscopy, *Biochim. Biophys. Acta (BBA)-Biomembranes*, 2018, **1860**, 1253–1258.
- 59 A. I. Cowen-Rivers, W. Lyu, R. Tutunov, Z. Wang, A. Grosnit, R. R. Griffiths, A. M. Maraval, H. Jianye, J. Wang and J. Peters, HEBO: Pushing The Limits of Sample-Efficient Hyper-parameter Optimisation, *J. Artif. Intell. Res.*, 2022, **74**, 1269–1349.



# Deep Learning (DL) for NRB removal in CARS Spectroscopy

## Page 4 Physical Chemistry Chemical Physics



CARS  
Spectrum

DL model architecture  
(CNN/ LSTM/ Bi-LSTM/ Autoencoder)

Raman  
spectrum